Seismological evidence for girdled olivine lattice-preferred orientation in oceanic lithosphere and implications for mantle deformation processes during seafloor spreading

J. B. Russell[1], J. B. Gaherty[2], H. F. Mark[3], G. Hirth[1], L. N. Hansen[4], D. Lizarralde[3], J. A. Collins[3], R. L. Evans[3]

[1]Department of Earth, Environmental and Planetary Sciences, Brown University, Providence, RI, USA.

[2]School of Earth and Sustainability, Northern Arizona University, Flagstaff, Arizona, USA.

[3]Woods Hole Oceanographic Institution, Woods Hole, MA, USA

[4]Department of Earth and Environmental Sciences, University of Minnesota, Minneapolis, MN, USA

Key Points:

- We develop an *in situ* elastic tensor for oceanic lithosphere that incorporates co-located compressional and shear anisotropy constraints
- Seismic anisotropy is consistent with corner flow during spreading and shear strains of 250–400%
- Girdled D-type olivine fabric implies activation of multiple olivine easy slip systems during mid-ocean ridge spreading

Corresponding author: J. B. Russell, Joshua_Russell@brown.edu

–1–

Abstract

Seismic anisotropy produced by aligned olivine in oceanic lithosphere offers a window into mid-ocean ridge dynamics. Yet, interpreting anisotropy in the context of grain-scale deformation processes and strain observed in laboratory experiments and natural olivine samples has proven challenging due to incomplete seismological constraints and length scale differences spanning orders of magnitude. To bridge this observational gap, we estimate an *in situ* elastic tensor for oceanic lithosphere using co-located compressional- and shear-wavespeed anisotropy observations at the NoMelt experiment located on $\sim$ 70 Ma seafloor. The elastic model for the upper 7 km of the mantle, NoMelt_SPani7, is characterized by a fast azimuth parallel to the fossil-spreading direction, consistent with corner-flow deformation fabric. We compare this model with a database of 123 petrofabrics from the literature to infer olivine crystallographic orientations and shear strain accumulated within the lithosphere. Direct comparison to olivine deformation experiments indicates strain accumulation of 250–400% in the shallow mantle. We find evidence for D-type olivine lattice-preferred orientation (LPO) with fast [100] parallel to the shear direction and girdled [010] and [001] crystallographic axes perpendicular to shear. D-type LPO implies similar amounts of slip on the (010)[100] and (001)[100] easy slip systems during mid-ocean ridge spreading; we hypothesize that grain-boundary sliding during dislocation creep relaxes strain compatibility, allowing D-type LPO to develop in the shallow lithosphere. Deformation dominated by dislocation-accommodated grain-boundary sliding (disGBS) has implications for *in situ* stress and grain size during mid-ocean ridge spreading and implies grain-size dependent deformation, in contrast to pure dislocation creep.

Plain Language Summary

Earth's upper mantle is composed primarily of the mineral olivine, which responds to deformation by organizing its seismically fast axis in the flow direction. During seafloor spreading, olivine crystals align with the spreading direction and become frozen into the lithosphere preserving the near-ridge deformation history. The resulting rock fabric can be observed in place via the directional dependence of seismic wavespeeds (seismic anisotropy) as well as in hand-sample rocks collected from the field. However, interpreting seismic anisotropy observations in the context of laboratory and field data remains a challenge, due to large differences in length scale and incomplete seismic constraints. Here, we bridge this observational gap by incorporating multiple data types to solve for the complete anisotropic

structure of oceanic lithosphere that formed ∼70 Myr ago. By comparing our model to laboratory data, we infer the magnitude of shear strain and style of olivine deformation during seafloor spreading for the first time. Our results indicate large shear strains and an olivine fabric type different to that typically assumed, implying the deformation is sensitive to the presence of grain boundaries even though most of the strain is produced by dislocations. This has new implications for the formation and evolution of oceanic plates.

1 Introduction

Observations of seismic anisotropy in the ocean basins provide unparalleled insight into Earth's mantle circulation patterns, including the plate-tectonic process of seafloor spreading (Hess, 1964; Forsyth, 1975; Nishimura & Forsyth, 1989; Montagner & Tani-moto, 1991; Gaherty et al., 2004; Toomey et al., 2007; Lin et al., 2016; Takeo et al., 2018; Mark et al., 2019). Based on olivine lattice-preferred orientation (LPO) observed in peri-dotites sampled from ophiolites and oceanic settings (Peselnick & Nicolas, 1978; Ben-Ismail & Mainprice, 1998; Michibayashi et al., 2006; Warren et al., 2008; Skemer et al., 2010) and in deformation experiments on olivine (Zhang & Karato, 1995; Zhang et al., 2000; Bystricky et al., 2000), upper-mantle anisotropy has historically been interpreted as evidence that deformation associated with mantle convection and plate tectonics oc-curs via dislocation creep in an olivine-rich upper mantle (Karato & Wu, 1993). This inference in turn has implications for key physical parameters such as grain size and stress, and more generally, the rheology of the upper mantle (Hirth & Kohlstedt, 2003).

Subsequent advances in laboratory deformation experiments on olivine have com-plicated this interpretation, however, illuminating variations in the activity of several olivine slip systems and associated LPO fabric types that may depend on mantle conditions such as stress, volatile content, and partial melting (Bystricky et al., 2000; Jung & Karato, 2001; Katayama et al., 2004; Jung et al., 2006; Qi et al., 2018). The three most commonly observed types of olivine LPO in experiments and natural settings are A-, E-, and D-type, each with their fast [100] crystallographic axis oriented sub-parallel to the shear direction but with variable orientations of the slow [010] and intermediate [001] axes (Fig-ure 1). Due to incomplete constraints on *in situ* shear and compressional velocities, it has not been possible to distinguish between these three fabric types in oceanic litho-

–3–

81 sphere using traditional seismological observations, leading to renewed ambiguity of phys-

82 ical state and deformation processes during seafloor spreading (Karato et al., 2008).

83 Here, we utilize a unique set of co-located shear and compressional anisotropy ob-

84 servations in the central Pacific (Mark et al., 2019; Russell et al., 2019) to produce an

85 exceptionally complete estimate of peridotite elasticity in the oceanic lithosphere. This

86 new seismic model, NoMelt_SPani, is then combined with a database of 123 olivine petro-

87 fabrics reported in the literature from experimentally and naturally deformed rocks to

88 constrain olivine LPO type and to quantify shear strain associated with seafloor spread-

89 ing near the mid-ocean ridge (MOR). The collection of laboratory and field petrofab-

90 ric observations provide a framework for quantitative interpretation of the *in situ* elas-

91 ticity tensor in terms of degree of strain, composition, LPO type, and potentially defor-

92 mation mechanism.

2 Data

2.1 Seismic observations at the NoMelt experiment

95 The NoMelt geophysical experiment in the central Pacific provided unique co-located

96 compressional- and shear-wave constraints (V_P and V_S, respectively) on *in situ* lithosphere

97 petrofabric over a 600×400 km^2 footprint with average seafloor age of $\sim$70 Ma. It com-

98 prised a refraction survey that constrained V_{PH} and its azimuthal anisotropy in the up-

99 per $\sim$7 km of the mantle (Mark et al., 2019) and a broadband ocean-bottom seismome-

100 ter deployment that resolved the complete V_S structure via observations of both Rayleigh-

101 wave (Lin et al., 2016) and Love-wave azimuthal anisotropy (Russell et al., 2019) in the

102 upper 40 km of the lithosphere. Together, these independent compressional and shear

103 observations of seismic anisotropy probe the complete elastic tensor of oceanic lithosphere.

2.2 Olivine fabric database

105 We have compiled a database of the elastic properties of 123 published olivine fab-

106 rics that includes 91 olivine samples deformed in the laboratory in direct shear (Zhang

107 & Karato, 1995; Jung & Karato, 2001; Katayama et al., 2004; Jung et al., 2006) and high-

108 strain torsion (Bystricky et al., 2000; Hansen et al., 2014, 2016) experiments, as well as

109 31 natural peridotite samples from diverse settings including ophiolites (Peselnick & Nico-

110 las, 1978; Ben-Ismail & Mainprice, 1998; Michibayashi et al., 2006; Warren et al., 2008;

Skemer et al., 2010), volcanic arcs (Mehl et al., 2003), and xenoliths and kimberlites from continental cratons (Ben-Ismail et al., 2001; Satsukawa et al., 2010). Of these samples, 42 (31 natural and 11 laboratory) have had LPO identified by the authors based on the orientations of their crystallographic axes: 12 have been identified as A-type, 6 E-type, and 24 D-type. The methods employed by these previous authors to calculate bulk seismic properties from individual crystallographic orientations generally follow a similar procedure and (1) nearly ubiquitously assume samples are composed of 100% olivine and (2) use the single-crystal olivine tensor of Abramson et al. (1997). For one harzburgite sample from the Oman ophiolite, the seismic properties were measured directly using ultrasonics, and therefore, contributions from other phases are inherently included (Peselnick & Nicolas, 1978). The temperature and pressure at which the elastic calculations are carried out can vary slightly among studies, but this has a negligible effect on seismic anisotropy (Ben-Ismail & Mainprice, 1998).

For all samples considered, the orientation of the elastic tensor with respect to the shear plane and shear direction were determined. Upon comparing to the seismic model, all samples in the database were oriented in the seismic reference frame: shear plane parallel to the X-Y plane defined by Earth's surface and shear direction parallel to the X-axis defined by the fossil-spreading direction (FSD). The Z-axis is oriented perpendicular to Earth's surface (i.e., perpendicular to the shear plane).

Estimates of shear strain associated with deformation are routinely measured for laboratory samples and range from undeformed ($\gamma \sim 0$) to $\gamma \sim 18.7$ in our dataset, but such estimates are rarely available for natural rocks. One exception is the Josephine shear zone in southwestern Oregon (Warren et al., 2008; Hansen & Warren, 2015), which has pre-existing foliations that provide passive strain markers that imply highly strained peridotites up to $\gamma \sim 20$ (Skemer et al., 2010).

3 Methods

3.1 Surface-wave inversion with P_n constraints

We invert previously measured surface-wave phase velocities for the shear and compressional velocities and anisotropy beneath the NoMelt array. Previously measured anisotropic Rayleigh- (5–150 s) and Love-wave (5–7.5 s) phase velocities from Russell et al. (2019) are inverted, while simultaneously satisfying V_P constraints in the upper $\sim$7 km of the

142 mantle from Mark et al. (2019) ("Weighted data, with gradients" in their Table 1). For

143 consistency, the inversion is carried out to 400 km depth as in Russell et al. (2019), but

144 we focus here only on the upper ∼7 km of the mantle, for which both P and S constraints

145 exist.

146   Surface-waves traveling through a weakly anisotropic medium with orthorhombic

147 symmetry can be described by 13 independent elastic parameters, composing the elas-

148 tic stiffness tensor, C_{ij}. Following Russell et al. (2019), we divide the elastic tensor into

149 two parts and invert for each separately:

$$C_{ij} = C_{ij}^{\mathrm{TI}} + \delta C_{ij} \,, \tag{1}$$

150 where C_{ij}^{TI} is the transversely isotropic part that consists of Love's five elastic param-

151 eters A, C, F, L, and N (Dziewonski & Anderson, 1981) describing azimuthally aver-

152 aged Rayleigh- and Love-wave phase velocities, and δC_{ij} contains eight parameters (G_{c},

153 G_{s}, B_{c}, B_{s}, E_{c}, E_{s}, H_{c}, H_{s}) that describe the strength and direction of azimuthal anisotropy

154 of Rayleigh and Love waves (see Appendix A).

155   First, we jointly invert the azimuthally averaged Rayleigh- and Love-wave phase

156 velocities (c^{R}, c^{L}) for the five transverse isotropy parameters $V_{\mathrm{SV}} = \sqrt{L/\rho}$, $V_{\mathrm{SH}} = \sqrt{N/\rho}$,

157 $V_{\mathrm{PV}} = \sqrt{C/\rho}$, $V_{\mathrm{PH}} = \sqrt{A/\rho}$, and $\eta = F/(A - 2L)$ (Dziewonski & Anderson, 1981):

$$\delta c^{\mathrm{R}}(\omega) = \frac{c^2}{U} \int \left(K_{\mathrm{PV}} \delta V_{\mathrm{PV}}(r) + K_{\mathrm{PH}} \delta V_{\mathrm{PH}}(r) + K_{\mathrm{SV}} \delta V_{\mathrm{SV}}(r) + K_\eta \delta\eta(r) \right) dr \,, \tag{2}$$

$$\delta c^{\mathrm{L}}(\omega) = \frac{c^2}{U} \int \left(K_{\mathrm{SV}} \delta V_{\mathrm{SV}}(r) + K_{\mathrm{SH}} \delta V_{\mathrm{SH}}(r) \right) dr \,, \tag{3}$$

158 where $\delta c(\omega) = c_0(\omega) - c^{\mathrm{pre}}(\omega)$ is the residual between observed and predicted isotropic

159 phase velocity at angular frequency ω at a given model iteration, U is group velocity, and

160 $K_m(\omega, r)$ are the Fréchet derivatives for each model parameter m calculated using MI-

161 NEOS. Poorly resolved parameters are scaled following Russell et al. (2019). We fix $\eta =$

162 $F/(A - 2L)$ to PREM values (Dziewonski & Anderson, 1981), and V_{PV} is scaled such

163 that $\phi^{-1} = (V_{\mathrm{PH}}/V_{\mathrm{PV}})^2$ remains equal to $\xi = (V_{\mathrm{SH}}/V_{\mathrm{SV}})^2$. In the upper 7 km of the

164 mantle, we fix V_{PH} to values from Mark et al. (2019). Radial anisotropy, ξ, provides a

165 proxy for the fast axis alignment in the horizontal ($\xi > 1$) or vertical ($\xi < 1$) plane.

166   Using the transversely isotropic model, we then invert the magnitude and fast az-

167 imuth of Rayleigh- and Love-wave azimuthal anisotropy for the depth dependent mag-

168 nitude and direction of azimuthal anisotropy elastic parameters G, B, H, and E (see Ap-

169 pendix A). Expressed in terms of sine and cosine coefficients A_{s} and A_{c}, respectively,

170 the relationships between surface-wave azimuthal anisotropy and the eight elastic pa-

171 rameters are given by (Montagner & Nataf, 1986)

$$A_{\mathrm{c2,s2}}^{\mathrm{R}}(\omega) = \frac{c}{U} \int \left(L\, K_L\, \frac{G_{\mathrm{c,s}}}{L}(r) + A\, K_A\, \frac{B_{\mathrm{c,s}}}{A}(r) + F\, K_F\, \frac{H_{\mathrm{c,s}}}{F}(r) \right)\, dr \,, \tag{4}$$

$$A_{\mathrm{c2,s2}}^{\mathrm{L}}(\omega) = \frac{c}{U} \int \left(-L\, K_L\, \frac{G_{\mathrm{c,s}}}{L}(r) \right)\, dr \,, \tag{5}$$

$$A_{\mathrm{c4,s4}}^{\mathrm{L}}(\omega) = \frac{c}{U} \int \left(-N\, K_N\, \frac{E_{\mathrm{c,s}}}{N}(r) \right)\, dr \,, \tag{6}$$

172 where subscripts containing '2' and '4' indicate 2θ and 4θ azimuthal variations and su-

173 perscripts again indicate wave type.

174   P_{n} waves sample V_{PH} directly beneath the Moho. The azimuthally averaged P_{n}

175 velocity and its 2θ and 4θ azimuthal dependence provides independent constraints on

176 elastic parameters A, B, and E, respectively via

$$\rho V_{P\mathrm{n}}(\theta)^2 = A + B_{\mathrm{c}} \cos(2\theta) + B_{\mathrm{s}} \sin(2\theta) + E_{\mathrm{c}} \cos(4\theta) + E_{\mathrm{s}} \sin(4\theta) \tag{7}$$

177 and enters the surface-wave inversion simply as prior constraints on those parameters.

178 Below $\sim$7 km beneath the Moho, at which P_{n} constraints terminate, and for the param-

179 eter H (which is poorly constrained by surface waves), we follow the general scaling ap-

180 proach described in Russell et al. (2019), whereby B and H scale directly with G. For

181 this study, the direct B and G constraints in the upper 7 km suggest an empirical B/G

182 scaling of $\sim$1.5 that is applied throughout the model. Additionally, an H/G scaling of

183 -0.11 is applied based on ophiolite samples (Peselnick & Nicolas, 1978; Ben-Ismail & Main-

184 price, 1998). The precise scaling between anisotropic parameters is complex and likely

185 depends on several factors including LPO symmetry, fabric orientation relative to the

186 horizontal plane, and the LPO of secondary phases (Montagner & Anderson, 1989). Thus,

187 this study focuses on G, B, E, and ξ in the shallowmost lithosphere for which these pa-

188 rameters are directly constrained by the seismic observations and do not depend on *a*

189 *priori* scaling assumptions.

₁₉₀ **3.2 Constructing the orthorhombic elastic tensor**

₁₉₁ A general elastic tensor is described by 21 independent elastic parameters. This

₁₉₂ tensor is simplified to only 9 parameters (A, C, F, L, N, G, B, H, E) if orthorhombic

₁₉₃ symmetry is assumed and the three orthogonal crystallographic axes ([100], [010], [001])

₁₉₄ are oriented along the principal directions (i.e., in the principal coordinate system). In

₁₉₅ this configuration, any crystallographic axis may be oriented along any of the three prin-

₁₉₆ cipal directions. This requirement is relaxed for the two horizontal directions in order

₁₉₇ to allow for arbitrary orientations of azimuthal anisotropy in the horizontal plane, re-

₁₉₈ sulting in an elastic tensor with 13 parameters (Montagner & Nataf, 1986). As one axis

₁₉₉ is assumed to be vertical (a requirement given that surface waves are horizontally prop-

₂₀₀ agating), dipping fabrics are not explicitly resolvable. The symmetric elastic tensor is

₂₀₁ given by

$$
C_{ij} = \begin{pmatrix}
A + B_{\rm c} + E_{\rm c} & A - 2N - E_{\rm c} & F + H_{\rm c} & 0 & 0 & \frac{1}{2}B_{\rm s} + E_{\rm s} \\
\cdot & A - B_{\rm c} + E_{\rm c} & F - H_{\rm c} & 0 & 0 & \frac{1}{2}B_{\rm s} - E_{\rm s} \\
\cdot & \cdot & C & 0 & 0 & H_{\rm s} \\
\cdot & \cdot & \cdot & L - G_{\rm c} & G_{\rm s} & 0 \\
\cdot & \cdot & \cdot & \cdot & L + G_{\rm c} & 0 \\
\cdot & \cdot & \cdot & \cdot & \cdot & N - E_{\rm c}
\end{pmatrix} . \quad (8)
$$

₂₀₂ Although we solve for all 13 parameters of the tensor in the upper 7 km of the mantle,

₂₀₃ only 9 are independently determined by our observations (L, N, A, $G_{\rm c,s}$, $B_{\rm c,s}$, $E_{\rm c,s}$). The

₂₀₄ remaining four terms that require scaling assumptions (C, F, $H_{\rm c,s}$) do not contribute

₂₀₅ to the quantitative comparisons between the *in situ* tensor and the natural and labo-

₂₀₆ ratory petrofabrics in Section 4.

3.3 Accounting for pyroxene in anisotropy calculations

Secondary phases other than olivine in a given sample act to reduce the bulk strength of seismic anisotropy (Mainprice & Silver, 1993; Bernard et al., 2021), yet the laboratory and natural petrofabrics used in this study consider aggregates of pure olivine. In order to directly compare these samples against our *in situ* estimate, which inherently includes bulk chemistry, we approximate the influence of secondary phases on seismic anisotropy following Hansen et al. (2014). Mineral physics calculations using the tool Perple_X (Connolly, 2009) suggest the shallow lithospheric mantle is comprised of ∼60 vol.% olivine assuming an upper mantle composition consistent with standard depleted mid-ocean ridge basalt (MORB) mantle composition (Hacker, 2008) and a half-space cooling temperature profile for 70 Ma (Figure S1). Invoking the simplifying assumption that the remaining 40% by volume can be approximated by orthopyroxene, a composite elastic tensor is constructed for each sample by taking the Voigt average between the olivine tensor and an orthopyroxene texture from Hansen et al. (2014) (Figure S2). This orthopyroxene texture comes from samples in which the orthopyroxene is dispersed in a dominantly olivine matrix, with the orthopyroxene comprising <3% of the total volume. We do not account for more complex structures, such as pyroxene-rich bands, which may develop in realistic polyphase aggregates with higher modal fractions of pyroxene. This treatment of the influence of orthopyroxene acts to reduce the overall strength of the fabric without having a large effect on the fast propagation azimuth (Bernard et al., 2021).

For samples in which author-reported anisotropy strengths were used instead of being calculated from an elastic tensor, an empirical scaling was applied to account for the effect of pyroxene. Considering only well-developed fabrics with $\gamma > 2$ from the laboratory data of Hansen et al. (2014, 2016), fabric strength was calculated with orthopyroxene content ranging from 0% to 100% by volume for each sample and was fit with a linear function (Figure S3). The relationship between pyroxene content and anisotropy magnitude is nearly -1:1 and provides a straightforward method for scaling anisotropy magnitude.

4 Results

4.1 A comprehensive elastic model of oceanic lithosphere

Previously measured high-frequency ambient-noise Rayleigh- and Love-wave phase velocities were inverted for the complete elastic structure at NoMelt, incorporating co-located P_{n} constraints. The resulting model, NoMelt_SPani, is shown in Figure 2, and here we focus on the upper ~7 km beneath the Moho for which P- and S-constraints co-incide. Azimuthal anisotropy increases with depth beneath the Moho for both G (V_{SV} anisotropy) and B (V_{PH} anisotropy), but remains relatively constant for E (V_{SH} anisotropy), largely due to the lack of Love-wave depth sensitivity (Russell et al., 2019). Anisotropy fast azimuths Ψ_{G} and Ψ_{B} are sub-parallel to the fossil-spreading direction (FSD), and Ψ_{E} is rotated by 45°, as predicted for orthorhombic olivine (Montagner & Nataf, 1986). In detail, while Ψ_{G} and Ψ_{B} are each consistent with FSD within error, they differ from one another by 5–10°. This subtle mismatch is likely attributed to the different depth sensitivities of P_{n} and surface waves: the refraction imaging is primarily sensitive to the shallowest ~7 km of the mantle, while the surface waves integrate across the upper ~20 km.

From the 13 elastic parameters, we construct the equivalent orthorhombic elastic tensor at each depth and average the upper 7 km to produce a single representative elas-tic tensor, NoMelt_SPani7, given in Table 1. The tensor has been rotated into the seis-mic reference frame such that X is parallel to the FSD, Y is perpendicular to the FSD and parallel to Earth's surface, and Z is perpendicular to Earth's surface. The V_{P} pole figure shown in Figure 2c indirectly expresses the relative orientations of the three crys-tallographic axes. The well-defined maximum parallel to the FSD indicates a sub-horizontal, clustered [100] fast axis. The girdled slow and intermediate directions indicate dispersed [010] and [001] axes perpendicular to the inferred shear direction, characteristic of D-type olivine fabric (Figure 1b).

4.2 Quantification of *in situ* strain

Olivine LPO strength, and in turn the magnitude of seismic anisotropy, increases with shear strain (Hansen et al., 2014, 2016). The NoMelt model provides four indepen-dent estimates of the magnitude of seismic anisotropy and three independent estimates of anisotropic directions that can be directly compared to olivine LPO formed as a func-tion of shear strain (Figure 3). We compare NoMelt_SPani7 to samples deformed in lab-

–10–

266 oratory torsion experiments (Hansen et al., 2014, 2016) as well as to samples deformed

267 naturally in a shear zone in the Josephine Peridotite, for which strain was determined

268 measurable in outcrop (Warren et al., 2008; Hansen & Warren, 2015).

269   When 100% olivine is assumed, the high strains required to match the orientation

270 of fast directions in Figure 3f–h correspond to magnitudes of anisotropy in Figure 3a–

271 d that are approximately twice that which we observe. As the NoMelt model represents

272 harzburgitic oceanic lithosphere, it is not surprising that a direct comparison to pure olivine

273 fabrics fails to produce a range of shear strains compatible with the seismic model. In-

274 corporating the effect of composition on the sample fabrics by accounting for the pres-

275 ence of pyroxene helps resolve this discrepancy. For each sample, we approximate the

276 contributions from pyroxene by combining each pure olivine elastic tensor with the ten-

277 sor for an appropriately oriented orthopyroxene texture following Hansen et al. (2014)

278 as described in Section 3.3. We assume a nominal harzburgite composition of 60% olivine

279 and 40% orthopyroxene by volume, which represents the lower bound of olivine content

280 in abyssal peridotites observed globally (Warren, 2016). For the natural samples from

281 Hansen & Warren (2015), dunite samples are used for the 100% olivine case, while harzbur-

282 gite samples with 40% orthopyroxene added are used for the 60% olivine case. This com-

283 position is also consistent with the average lithospheric V_P and V_S in the NoMelt model,

284 as compared to Perple_X calculations (Connolly, 2009) for a typical depleted mid-ocean

285 ridge basalt (Figure S1). Compared to the pure olivine estimates, the mixture system-

286 atically decreases the strength of anisotropy due to the weaker single-crystal anisotropy

287 and LPO of orthopyroxene compared to olivine (Mainprice & Silver, 1993), while fast

288 azimuths are largely unaffected. This observation is consistent with the recent findings

289 of Bernard et al. (2021), who investigated orthopyroxene effects on seismic anisotropy

290 using a large suite of upper mantle xenoliths and found that the fast azimuth of anisotropy

291 is not affected by orthopyroxene LPO for samples with >60% olivine.

292   The overall agreement between NoMelt anisotropy and the laboratory torsion data

293 for 60% olivine is remarkable given the vast difference in length scale of the measurements

294 (∼9 orders of magnitude assuming seismic wavelengths on the order of ∼100 km and lab-

295 oratory LPO texture measurements from areas of ∼100×100 μm^2). The magnitude of

296 anisotropy at NoMelt is consistent with laboratory samples for shear strains ranging from

297 approximately 2 to 4 (minimum average misfit at $\gamma = 2.7$), and the orientation of fast

298 directions is consistent with $\gamma > 3$ (Figure 4). We therefore infer that this portion of

–11–

²⁹⁹ the upper mantle was subject to shear strains ranging from 2.5 to 4, which is on the up-

³⁰⁰ per end of that expected at shallow depths during seafloor spreading (Tommasi, 1998).

³⁰¹ The angle between the fast V_P axis and inferred shear plane is small ($\lesssim 10°$) for $\gamma >$

³⁰² 1.5 (Figure 3e), implying a sub-horizontal concentration of [100] crystallographic axes

³⁰³ (Skemer et al., 2012). Based on this observation we interpret a subhorizontal fabric at

³⁰⁴ NoMelt, although we are unable to directly constrain fabric dip with our dataset that

³⁰⁵ consists only of horizontally propagating waves.

³⁰⁶   In natural samples, the evolution of LPO with increasing strain is more scattered

³⁰⁷ and exhibits clear differences compared to experimental samples. For a given strain and

³⁰⁸ olivine content, the magnitude of anisotropy of the natural fabrics is consistently weaker.

³⁰⁹ This is perhaps unsurprising given the differences in scale between natural shear zones,

³¹⁰ such as at the Josephine ophiolite, and laboratory torsion experiments. In addition, the

³¹¹ anisotropy fast directions of the natural samples fail to consistently rotate into the shear

³¹² direction with increasing strain, remaining misaligned by $\sim25°$ at $\gamma = 5.25$ (Figure 3f–

³¹³ h). The relatively weak and misaligned anisotropy of the highly strained Josephine sam-

³¹⁴ ples is likely attributed to the presence of a pre-existing LPO prior to shear zone devel-

³¹⁵ opment, which prolongs fabric development and misalignment of [100] with respect to

³¹⁶ the shear direction (Warren et al., 2008; Skemer et al., 2012; Kumamoto et al., 2019).

³¹⁷ The natural samples also include contributions of secondary phases to LPO development,

³¹⁸ while the laboratory experiments on pure olivine do not. Uncertainties associated with

³¹⁹ measuring orientations in the field and preparing oriented samples for electron backscat-

³²⁰ ter diffraction (EBSD) measurements in the lab may also contribute to scatter. NoMelt

³²¹ anisotropy is stronger than even the most highly strained natural sample ($\gamma = 5.25$)

³²² with 60% olivine, highlighting the remarkably coherent LPO in the lithosphere across

³²³ the 600×400 km^2 NoMelt footprint (Russell et al., 2019). Any pre-existing vertical LPO

³²⁴ associated with upwelling at the ridge was likely weak in comparison to that imposed

³²⁵ after corner flow and therefore overprinted.

³²⁶   Strain evolution of LPO from D-type at intermediate strains to A-type at high strains

³²⁷ was previously identified by Hansen et al. (2014). This LPO evolution is reflected in the

³²⁸ average V_P surfaces shown above Figure 3a (see supplementary Figure S6). The inferred

³²⁹ shear strain at NoMelt of 2.5–4 based on strength and direction of anisotropy in com-

³³⁰ parison to laboratory samples corresponds to fabrics with girdled slow and intermedi-

³³¹ ate V_P directions on average, consistent with a D-type LPO.

<center>–12–</center>

4.3 Distinguishing LPO fabric type

We further investigate LPO fabric type by comparing the relative magnitudes of azimuthal and radial anisotropy, which provides a discriminant of LPO type if the orientation of the sample with respect to the shear plane is known (Karato et al., 2008; Karato, 2008) (Figure 1). The idea is similar to the more general Flinn diagram method of Michibayashi et al. (2016) based on ratios of V_P along different crystallographic directions and was recently proposed as a way to distinguish intrinsic LPO from extrinsic anisotropy mechanisms such as compositional layering or oriented melt pockets (Hansen et al., 2021). In Figure 5, we compare the strength of NoMelt anisotropy with that calculated for A-, D-, and E-type olivine fabrics from both natural settings (Peselnick & Nicolas, 1978; Ben-Ismail & Mainprice, 1998; Ben-Ismail et al., 2001; Mehl et al., 2003; Michibayashi et al., 2006; Warren et al., 2008; Karato, 2008; Skemer et al., 2010; Satsukawa et al., 2010) and laboratory deformation experiments (Zhang et al., 2000; Bystricky et al., 2000; Jung & Karato, 2001; Katayama et al., 2004; Jung et al., 2006). For most samples, the LPO type was characterized by the original authors.

To first order, samples with A-type LPO tend to exhibit strong radial anisotropy relative to azimuthal anisotropy, whereas the opposite is true for E-type. NoMelt displays moderate radial and azimuthal anisotropy most similar to the samples with D-type LPO. This result holds regardless of the olivine content assumed (Figure S4), though we find that a composition of 75% olivine and 25% orthopyroxene provides the best overall fit to the seismic observations. As the D-type LPO data in Figure 5 represent mostly natural samples, the higher olivine content required to match the seismic model is consistent with Figure 3, which showed that natural samples underestimate the magnitude of anisotropy for 60% olivine and 40% orthopyroxene. The true pyroxene content of the Josephine harzburgites ranges between 12.8–35.1% (Hansen & Warren, 2015), and accounting for this fact would bring the natural samples closer to the NoMelt observations of B/A, G/L, and E/N in Figure 3. A harzburgite composition with 75% olivine is also consistent with abyssal peridotites from fast-spreading MORs, which tend to have higher olivine content (70–95%) compared to slow-spreading MORs (Dick & Natland, 1996; Niu & Hékinian, 1997; Warren, 2016). If lower pyroxene content is assumed, the relationship in Figure 3a–d would indicate a moderately lower magnitude of strain at NoMelt that is inconsistent with the higher strains implied by the anisotropy fast orientations parallel to the shear direction (Figure 3f–h).

365   Scatter among samples of the same fabric type in Figure 5 is likely attributed to

366 differences in shear strain, with low strain samples exhibiting weaker anisotropy, as demon-

367 strated in Figure 3a–d. At lower shear strains (and in the presence of a pre-existing LPO)

368 dip of [100] with respect to the shear plane is common (Skemer et al., 2012) (Figure 3e),

369 resulting in weaker radial and azimuthal anisotropy. Therefore, dipping fabrics in Fig-

370 ure 5 will tend to skew towards the origin, which does not change the overall inference

371 of D-type LPO (see supplementary Figure S5). In other cases, scatter may be attributed

372 to samples that straddle the boundary between two LPO types, such as the peridotite

373 averages of Ben-Ismail & Mainprice (1998), which included both A-type and D-type sam-

374 ples.

5 Discussion

376   This study presents, to our knowledge, the first *in situ* quantification of the orthorhom-

377 bic elastic tensor of oceanic lithosphere that incorporates both compressional- and shear-

378 anisotropy observations at a single location. The model, NoMelt_SPani7, represents typ-

379 ical oceanic lithosphere produced by corner flow at a fast-spreading MOR, providing a

380 benchmark for LPO formation during seafloor spreading. The relatively simple corner-

381 flow geometry followed by strain accumulation with horizontal flow lines allows for straight-

382 forward comparison with deformed olivine petrofabrics from both natural and labora-

383 tory settings. Under the assumption of horizontal shear, we are able to infer the accu-

384 mulation of shear strain in the upper 7 km of the mantle to be of order 250–400% (Fig-

385 ure 3), with [010] and [001] girdled perpendicular to the shear direction, characteristic

386 of D-type LPO (Figure 5).

5.1 Limitations of the seismic model

388   While this study provides an exceptionally complete *in situ* elastic model of oceanic

389 lithosphere, several limitations exist. First, we are unable to explicitly solve for fabric

390 dip because only horizontally propagating waves (surface waves and P_n) are used. The-

391 oretically, it is possible to utilize P and S body waves with a range of incidence angles

392 to constrain fabric dip via the zero-valued off-diagonal elements of C_{ij} (eq 8). In prac-

393 tice however, this is extremely challenging, requiring earthquake observations from a range

394 of epicentral distances and back-azimuths that have been effectively corrected for near-

395 source and deep-earth 3-D structure outside the region of interest. Our use of labora-

–14–

³⁹⁶ tory data to indirectly infer fabric dip based on the observation of fast azimuth align-

³⁹⁷ ment with the FSD suggests fabric is horizontal to within $\sim 10°$ in our study region, pro-

³⁹⁸ viding confidence in our current approach.

³⁹⁹ A consequence of D-type LPO is the inability to uniquely determine the orienta-

⁴⁰⁰ tion of the shear plane using seismologically determined crystallographic orientations alone.

⁴⁰¹ Fortunately, the assumption of a horizontal shear plane is valid for many plate-tectonic

⁴⁰² processes including MOR spreading once far enough from the ridge. Our ability to com-

⁴⁰³ pare the seismological model with natural and laboratory data in a relatively straight-

⁴⁰⁴ forward way is largely a result of the simple geometry. For more complex tectonic en-

⁴⁰⁵ vironments such as subduction zones or directly beneath MORs, the orientation of the

⁴⁰⁶ shear plane may be significantly rotated from horizontal, and this simplified approach

⁴⁰⁷ breaks down.

⁴⁰⁸ As our 1-D model represents an average over the 600×400 km^2 NoMelt footprint,

⁴⁰⁹ a variation in LPO type across the region cannot be completely ruled out. For instance,

⁴¹⁰ a spatial variation from A-type to E-type could appear as D-type LPO when averaged

⁴¹¹ over the array. Alternatively, averaging over domains with A-type LPO that have a com-

⁴¹² mon shear direction but orthogonal orientations of the shear planes could produce an

⁴¹³ apparent D-type LPO. This could be the case, for example, if averaging over oceanic litho-

⁴¹⁴ sphere that includes transform faults and fracture zones, which could incorporate tran-

⁴¹⁵ sitions between horizontal and vertical shear planes. However, NoMelt is situated be-

⁴¹⁶ tween the Clarion and Clipperton Fracture Zones on lithosphere formed at a single MOR

⁴¹⁷ segment, and therefore the model captures only normal seafloor-spreading fabric. In ad-

⁴¹⁸ dition, lateral variations in surface-wave phase velocities imaged at NoMelt are small ($<1\%$)

⁴¹⁹ (Russell et al., 2019), consistent with a homogeneous LPO type within the footprint.

5.2 Strain accumulation in the shallow lithosphere

⁴²¹ Our estimate of 250–400% strain accumulated in the upper 7 km of the mantle based

⁴²² on observed seismic anisotropy is, to our knowledge, the first of its type. The primary

⁴²³ assumption underlying this estimate is that the strain evolution of olivine LPO – and

⁴²⁴ in turn seismic anisotropy – observed in the laboratory is the same as that which occurs

⁴²⁵ in the mantle. This necessary assumption could be an oversimplification. The influence

⁴²⁶ of secondary phases, such as pyroxene, on the development of olivine LPO has not been

427 well quantified in laboratory experiments and may depend on the proportion of the sec-

428 ondary phase relative to olivine. In addition, if a pre-existing fabric forms during upwelling

429 at the MOR, LPO development associated with corner flow would be delayed, and strain

430 estimates based solely on seismic anisotropy would be underestimated (Skemer et al.,

431 2010). Therefore, we consider the range 250–400% to be a lower bound on strain accu-

432 mulated in the shallow lithosphere. Because the strength of LPO and seismic anisotropy

433 saturate at higher strains (Figure 3) (Tommasi, 1998; Tommasi & Vauchez, 2015), seis-

434 mic anisotropy is limited in its ability to quantify strains greater than ∼400%.

5.3 Interpretation of D-type fabric

436 The relative strengths of radial and azimuthal anisotropy in the shallow lithosphere

437 at NoMelt are consistent with that of D-type peridotites (Figure 5). As NoMelt is thought

438 to represent typical oceanic plate, this observation suggests that D-type LPO is widespread

439 in oceanic lithosphere. This hypothesis is supported by numerous studies that document

440 D-type LPO (in addition to A-type) in oceanic peridotites (e.g. Ben-Ismail & Mainprice,

441 1998; Tommasi et al., 2004; Michibayashi et al., 2006; Vonlanthen et al., 2006; Warren

442 et al., 2008; Michibayashi et al., 2016; Liu et al., 2019; Tommasi et al., 2020). Given our

443 result, we explore utilizing this constraint on fabric type to improve our understanding

444 of mantle deformation during seafloor spreading.

445 It has been well established from laboratory experiments (e.g. Karato et al., 1980;

446 Karato & Wu, 1993; Zhang & Karato, 1995), direct sampling (e.g. Peselnick & Nicolas,

447 1978; Ben-Ismail & Mainprice, 1998; Tommasi et al., 2004), and seismic observations (e.g.

448 Hess, 1964; Forsyth, 1975; Nishimura & Forsyth, 1989) that the olivine-rich upper man-

449 tle deforms via dislocation creep. This inference led to the common assumption that A-

450 type LPO pervades the upper mantle, as it primarily results from dislocation creep with

451 slip dominantly occurring on the easiest olivine slip system, (010)[100]. In contrast, D-

452 type LPO results from slip on both easy slip systems (010)[100] and (001)[100] (e.g. Bystricky

453 et al., 2000; Hansen et al., 2014). Single-crystal experiments demonstrate that critical

454 resolved shear stresses for (001)[100] are similar to (010)[100] for comparable strain rates

455 and temperatures $<1300°C$ (Bai et al., 1991).

456 Similar amounts of slip on both (001)[100] and (010)[100] are favored if the von Mises

457 strain compatibility criterion is relaxed, minimizing activity of the hardest slip system,

–16–

458 (010)[001] (Tommasi et al., 2000; Castelnau et al., 2008; Signorelli & Tommasi, 2015).

459 Several grain-scale mechanisms have been proposed for relaxing strain compatibility in

460 the oceanic lithosphere. On the one hand, numerical modeling suggests that subgrain

461 rotation recrystallization can relax the requirement for strain compatibility by increas-

462 ing intragranular strain heterogeneity (Signorelli & Tommasi, 2015). On the other hand,

463 laboratory studies indicate that von Mises criterion can be relaxed by grain-boundary

464 sliding during dislocation creep (Hirth & Kohlstedt, 2003; Hansen et al., 2011). Based

465 on the observed grain-size dependence, dislocation-accommodated grain-boundary slid-

466 ing (disGBS) has been observed to be the dominant dislocation-creep mechanism dur-

467 ing experiments on olivine aggregates over a wide range of stresses and grain sizes (Hansen

468 et al., 2011; Bollinger et al., 2019), including in higher temperature experiments that pro-

469 duced D-type fabric (e.g. Bystricky et al., 2000; Hansen et al., 2011). We emphasize that

470 a significant amount of strain — and accompanying grain rotations that lead to LPO

471 — is accommodated by dislocation glide on the easy slip systems in this disGBS regime,

472 even when processes at the grain boundaries are rate limiting (e.g., see Discussion in Fer-

473 reira et al., 2021). In other words, the disGBS mechanism can be understood as a form

474 of dislocation creep in which the dislocations interact with the grain boundaries, result-

475 ing in sensitivity to grain size.

476 DisGBS has been previously invoked to explain the occurrence of D-type LPO in

477 oceanic peridotites (Braun, 2004; Warren et al., 2008). In ophiolites, A- and D-type LPOs

478 have been observed in course-grained dunites and finer-grained harzburgites, respectively,

479 suggesting pyroxene may play a role in D-type LPO formation by limiting olivine grain

480 size and promoting deformation by disGBS (Warren et al., 2008). Indeed, contributions

481 from pyroxene are important for reconciling the NoMelt observation with sample data

482 more broadly (Figures 3,5).

483 Several recent studies have proposed that olivine LPO in the upper mantle may

484 be produced by diffusion creep, rather than dislocation creep or disGBS (Miyazaki et

485 al., 2013; Yabe & Hiraga, 2020). Yabe & Hiraga (2020) observed grain sizes in mantle

486 xenoliths from oceanic mantle lithosphere that follow the Zener relationship (Linckens

487 et al., 2011; Kim et al., 2022), which can lead to grain sizes smaller than produced by

488 steady state dynamic recrystallization — and therefore promote diffusion creep. Although

489 the pure-shear diffusion-creep experiments of Kim et al. (2022) produced only A-type

490 and AG-type LPO (girdled [100] and [001] within the shear plane), they predict that pro-

–17–

491 late ("cigar" shape) strain could promote the development of D-type LPO. However, such

492 constructional strain in not expected at the base of the plate during corner flow, espe-

493 cially at fast spreading rates.

494 To our knowledge, D-type LPO has been produced in the laboratory only at con-

495 ditions in which disGBS is the dominant deformation mechanism. While we cannot rule

496 out the possibility of D-type LPO developing without a contribution from grain-boundary

497 sliding, such a scenario has not been demonstrated in laboratory experiments. There-

498 fore, we consider disGBS a likely candidate for relaxing strain compatibility requirements

499 in the mantle. In the following section, we explore the implications of this hypothesis

500 recognizing that other mechanisms could contribute to D-type LPO formation.

5.3.1 Implications of the disGBS hypothesis

502 We examine the hypothesis that deformation via disGBS during MOR spreading

503 produced the D-type LPO that we observe in the oceanic lithosphere. Olivine flow laws

504 derived from laboratory experiments suggest that the disGBS process dominates at upper-

505 mantle conditions (Figure 6a). Similarly, MOR geodynamic modeling that incorporates

506 grain-size evolution and multiple deformation processes (diffusion creep, dislocation creep,

507 and disGBS) indicates that shallow, near-ridge deformation is dominated by disGBS in

508 some cases (Turner et al., 2015). These results have potentially important rheological

509 implications, as disGBS is essentially grain-size sensitive dislocation creep, while tradi-

510 tionally dislocation creep is considered to be insensitive to grain size (Hirth & Kohlst-

511 edt, 2003; Hansen et al., 2011). Here, we explore how upper-mantle grain size and stress

512 may influence the dominant deformation mechanism.

513 Olivine flow laws at a given temperature and pressure describe the strain-rate con-

514 tributions of grain-size insensitive dislocation creep, disGBS, and diffusion creep processes

515 as a function of stress and grain size. A deformation mechanism map is presented in Fig-

516 ure 6a for reasonable sub-Moho conditions at the MOR ($T = 1250°C$, $P = 360$ MPa),

517 using olivine flow-law parameters from Hansen et al. (2011) (Table S3). For a given stress,

518 grain-size insensitive dislocation creep dominates at large grain sizes, and diffusion creep

519 occurs at small grain sizes. The disGBS regime occupies the transition between the two

520 and is distinguished by its modest grain-size dependence.

521 Assuming tectonic strain rates of $10^{-14.5}$–$10^{-12.5}$ s^{-1}, deformation via disGBS im-
522 plies *in situ* grain sizes of 0.3–15 mm and relatively low stress (0.2–1.4 MPa), broadly
523 consistent with recent geodynamic modeling at a MOR (Turner et al., 2015, 2017) as well
524 as olivine grain sizes observed in peridotites (e.g. Vonlanthen et al., 2006; Tommasi et
525 al., 2020). However, these grain sizes are on the smaller end of the steady-state predic-
526 tions of ∼5–50 mm from the laboratory-calibrated grain-size piezometers (Karato et al.,
527 1980; Hirth & Kohlstedt, 2015) and the wattmeter (Austin & Evans, 2007) shown in Fig-
528 ure 6a (see Appendix Appendix B for details of wattmeter calculation).

529 Relatively small experimental uncertainties result in large uncertainties when ex-
530 trapolated to mantle conditions. Considering the uncertainty in the flow-law parame-
531 ters (see Appendix Appendix C for details), scenarios are possible in which the disGBS
532 field expands to larger grain sizes coinciding with the piezometer and wattmeter predic-
533 tions at mantle conditions while still satisfying the laboratory data (Figure 6b). Figure C1
534 shows the full range of possible flow-law parameter values (within experimental uncer-
535 tainties) for which disGBS is predicted to be the dominant deformation mechanism at
536 the stress/grain size values estimated by extrapolation of the grain size piezometer/wattmeter.
537 If disGBS is responsible for producing the D-type LPO we observe and the extrapola-
538 tion of the piezometer/wattmeter relationships are applicable, this analysis suggests that
539 the nominal olivine flow law of Hansen et al. (2011) underpredicts the contribution of
540 disGBS at mantle conditions, with a preference for smaller disGBS stress and grain-size
541 exponents n_{GBS} and m_{GBS}, respectively, and/or a larger dislocation creep stress expo-
542 nent n_{DISL} relative to their nominal reference values (Table S3).

543 Alternatively, it is possible that the flow-law parameters are skewed in the oppo-
544 site sense, such that disGBS does not occur at mantle conditions (Figure 6c) and defor-
545 mation occurs purely in the grain-size insensitive dislocation-creep regime. This scenario
546 would require an alternative mechanism for producing the evidence for D-type LPO; vis-
547 coplastic self-consistent models show scenarios in which dynamic recrystallization by sub-
548 grain rotation can produce a D-type LPO (Signorelli & Tommasi, 2015). Another pos-
549 sibility is that the nominal flow-law parameters in Figure 6a are valid, but the temper-
550 ature at which the LPO was acquired was significantly lower than 1250°C (see Figure S7)
551 and/or mantle grain sizes are somewhat smaller than predicted by the wattmeter and
552 piezometer. Indeed, olivine grain sizes in the range of 0.5–5 mm are commonly observed
553 in mantle peridotites (e.g. Vonlanthen et al., 2006; Michibayashi et al., 2006; Liu et al.,

–19–

2019; Tommasi et al., 2020). These grain sizes observed in nature sit squarely in our predicted disGBS field and may be due to grain-boundary pinning in the presence of secondary phases such as pyroxene, which is not captured by predictions based on results from olivine experiments. New experiments that place tighter bounds on olivine flow-law parameters and quantify contributions of pyroxene are required to resolve these ambiguities.

This discussion is not meant to invalidate a particular olivine flow law or mechanism for relaxing strain compatibility requirements in the oceanic lithosphere; rather, the purpose is to 1) highlight the uncertainties associated with extrapolating to mantle conditions across nearly two orders of magnitude in stress and grain size — small experimental uncertainties equate to large uncertainties at mantle conditions, 2) illustrate how *in situ* observations of LPO type may be utilized to better constrain such extrapolations, and 3) demonstrate that the disGBS hypothesis is *consistent* with grain sizes observed in mantle rocks, to within experimental uncertainty.

5.4 Mid-ocean ridge deformation

The strong correspondence between observed anisotropic fast directions and the direction of fossil seafloor spreading at NoMelt implies that the *in situ* elastic tensor represents mantle deformed by corner flow during spreading. Our inferences of girdled D-type LPO, high strain accumulation ($\gamma = 2.5$–4), and sub-horizontal [100] orientations will inform new geodynamic modeling efforts of MOR dynamics and associated fabric development. Recent models often contain relatively weak anisotropy in the shallow lithosphere with a dipping [100] orientation and A-type LPO (e.g. Blackman et al., 1996, 2017), in contrast to what we infer at NoMelt. Our observation of D-type LPO, implying equal amounts of slip on both (010)[100] and (001)[100] during MOR spreading, provides a new target for future geodynamic models. More girdled fabrics have been previously produced in viscoplastic self-consistent models by relaxing strain compatibility constraints (Tommasi et al., 2000), but generally such alternative LPO types are not explored in geodynamic models.

Rapid mantle flow in the direction of plate spreading that outpaces the spreading rate could enhance strain directly beneath the Moho relative to passive corner flow (Kodaira et al., 2014). Such active mantle flow patterns during crust and uppermost man-

tle lithosphere formation have been inferred from observations of lower crustal dipping reflectors and strong azimuthal anisotropy below the Moho in fast-spreading lithosphere (5–7 cm/yr) in the western Pacific (Kodaira et al., 2014) and offshore Alaska (Bécel et al., 2015). Russell et al. (2019) observed 4–5% radial anisotropy in the lower crust at NoMelt consistent with the presence of horizontal or gently dipping reflectors, but they were unable to resolve whether the anisotropy is produced by a shape-preferred orientation of lithological layering (mafic/ultramafic banding) or LPO produced by shearing. The former has been widely observed in the lower gabbroic sections of ophiolites (e.g. Smewing, 1981; Pallister & Hopson, 1981; Karson et al., 1984), while the latter has not been directly observed. Furthermore, V_P anisotropy in the upper ∼3 km of the mantle at NoMelt is relatively modest (6–7%) compared to observations in the western Pacific (8.5–9.8%) for which active mantle flow was invoked (Kodaira et al., 2014). This observation implies that if active mantle flow was present during formation of the NoMelt lithosphere ∼70 Ma, then it must have been relatively weak. Therefore, we favor the simpler interpretation that LPO was acquired primarily by passive corner flow.

Although the precise grain-scale mechanism(s) involved in reducing strain compatibility requirements is still uncertain, D-type LPO is consistent with shallow deformation via grain-size sensitive dislocation creep (i.e., disGBS). This would imply a complex, non-Newtonian and grain-size dependent rheology that impacts solid-state convection streamlines, melt extraction, and thermal and rheological evolution of the lithosphere and asthenosphere (Turner et al., 2017). Grain size, in particular, has been shown to play an important role in melt focusing near MORs through alteration of the viscosity structure resulting in gradients in compaction pressure (Turner et al., 2015, 2017). Smaller grain sizes in the shallow mantle required for disGBS (∼1–10 mm) would decrease porosity and permeability, acting as a permeability barrier along which melt may be focused towards the ridge axis. Although our modeling is only sensitive to the shallow lithospheric mantle, significantly shallower than where melt is stable off-axis, geodynamic models that include non-Newtonian viscosities predict that disGBS also dominates in the shallow asthenospheric mantle (Turner et al., 2015). Presence of melt near the ridge axis may inhibit grain growth, leading to decreased recrystallized grain size and further promoting the disGBS mechanism (Hirth & Kohlstedt, 1995; Faul, 1997; Braun et al., 2000).

⁶¹⁶ ## 5.5 Importance of pyroxene

⁶¹⁷   The influence of pyroxene on bulk anisotropy, LPO development, and mantle rhe-
⁶¹⁸ ology is still under investigation. A recent study of natural peridotites containing var-
⁶¹⁹ ious olivine and orthopyroxene LPO types shows that orthopyroxene has no significant
⁶²⁰ effect on the fast azimuth of seismic anisotropy when olivine composes at least 60% of
⁶²¹ the sample (Bernard et al., 2021). However, the strength of anisotropy does depend on
⁶²² both the proportion of pyroxene and the magnitude of strain (Figure 3a–d). In practice,
⁶²³ it is not possible to separate these two effects when composition is unknown, and one
⁶²⁴ must assume a realistic mantle composition based on prior knowledge as we have done.
⁶²⁵ Additionally, shear strain is not readily determined in natural samples except in special
⁶²⁶ cases for which strain markers are present, such as at the Josephine shear zone (War-
⁶²⁷ ren et al., 2008; Hansen & Warren, 2015), and those samples by definition contain a pre-
⁶²⁸ existing LPO, which also impacts strain development. Untangling these competing ef-
⁶²⁹ fects on anisotropy will require peridotite elastic tensors that account for the true modal
⁶³⁰ compositions and LPO for all main phases within the sample (e.g. Tommasi et al., 2004;
⁶³¹ Vonlanthen et al., 2006; Liu et al., 2019; Tommasi et al., 2020). In addition, high-strain
⁶³² experiments are needed that examine the effect of olivine and pyroxene together and that
⁶³³ quantify the influence of pre-existing fabric on LPO development using realistic aggre-
⁶³⁴ gate compositions.

⁶³⁵ # 6 Conclusions

⁶³⁶   We develop an *in situ* elastic tensor for ∼70 Ma oceanic lithosphere constrained
⁶³⁷ by co-located shear and compressional seismic observations sensitive to the upper ∼7 km
⁶³⁸ of the mantle. By comparing our model to a suite of previously published tensors from
⁶³⁹ olivine aggregates deformed in nature and in the laboratory, we provide new constraints
⁶⁴⁰ on LPO type and magnitude of shear strain accumulated in oceanic lithosphere. The rel-
⁶⁴¹ atively strong azimuthal anisotropy with fast azimuth parallel to the spreading direc-
⁶⁴² tion is consistent with shear strains of 250–400% and sub-horizontal fabric produced by
⁶⁴³ corner flow near the MOR. The relative strengths of azimuthal and radial anisotropy cor-
⁶⁴⁴ respond to D-type LPO ([100] parallel to the shear direction and girdled [001] and [010]
⁶⁴⁵ perpendicular to shear) irrespective of assumed olivine content or fabric dip. Assuming
⁶⁴⁶ NoMelt represents the average oceanic plate, this result implies that D-type LPO is more
⁶⁴⁷ ubiquitous in the oceanic lithosphere than typically thought. Our observations can be

⁶⁴⁸ explained by a mantle composition of 60–75% olivine, consistent with observed mantle

⁶⁴⁹ peridotites, but the competing effects of composition, strain, and pre-existing LPO on

⁶⁵⁰ anisotropy strength cannot be completely isolated.

⁶⁵¹ We hypothesize that D-type LPO in the shallow lithosphere results from near-ridge

⁶⁵² deformation dominated by disGBS that relaxes strain compatibility requirements and

⁶⁵³ produces equal amounts of slip on both easy slip systems. Under this assumption, our

⁶⁵⁴ observation implies *in situ* grain sizes of 0.3–15 mm, consistent with observed peridotites,

⁶⁵⁵ and stresses on the order of 0.2–1.4 MPa. The grain-size sensitivity of disGBS deforma-

⁶⁵⁶ tion impacts the rheological behavior of the spreading mantle and subsequent LPO de-

⁶⁵⁷ velopment. This study demonstrates the ability to integrate seismological- and laboratory-

⁶⁵⁸ scale observations of seismic anisotropy to improve understanding of MOR dynamics and

⁶⁵⁹ mantle deformation during seafloor spreading.
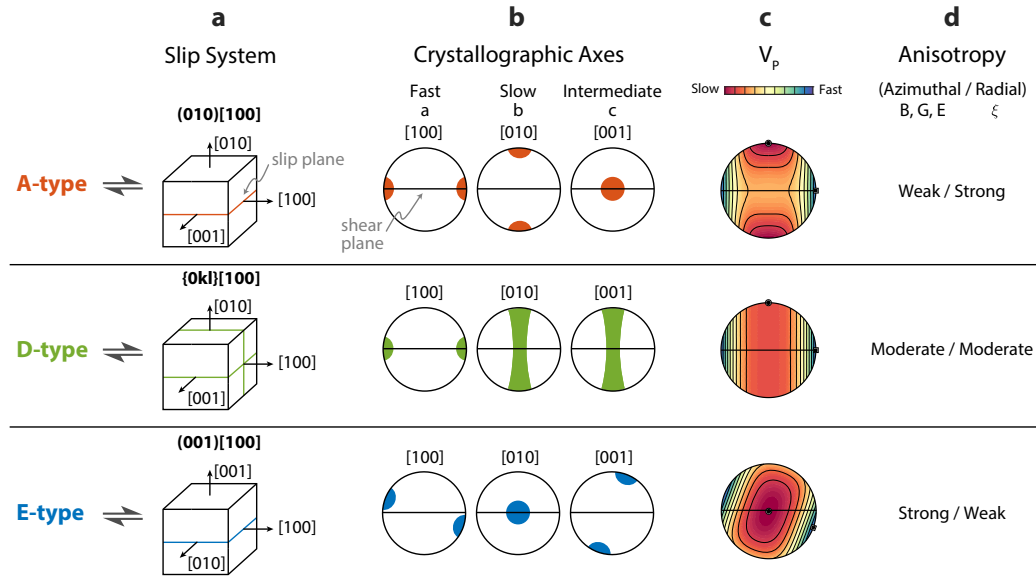
Figure 1. Schematic summary of the most commonly observed LPO types. (**a**) slip systems, (**b**) crystallographic orientations, and (**c**) compressional velocities, V_{P}, expected for right lateral shear (top to the right shear sense). Note the qualitative differences in V_{P} between the three fabric types arising from the relative orientations of [100], [010], and [001]. (**d**) Relative strengths of radial and azimuthal anisotropy for A-, D-, and E-type fabrics under the assumption that the shear plane is parallel to Earth's surface. Differences in the orientation of slow [010] and intermediate [001] axes result in measurable differences in seismic anisotropy. Azimuthal anisotropy is sensitive to the two crystallographic axes in the horizontal plane, and radial anisotropy is sensitive to the difference between the azimuthally averaged horizontal axes and the vertically oriented axis. The depiction of a slight rotation of [100] from the shear plane for E-type LPO is based on laboratory observations (Katayama et al., 2004) and natural samples (Skemer et al., 2010).
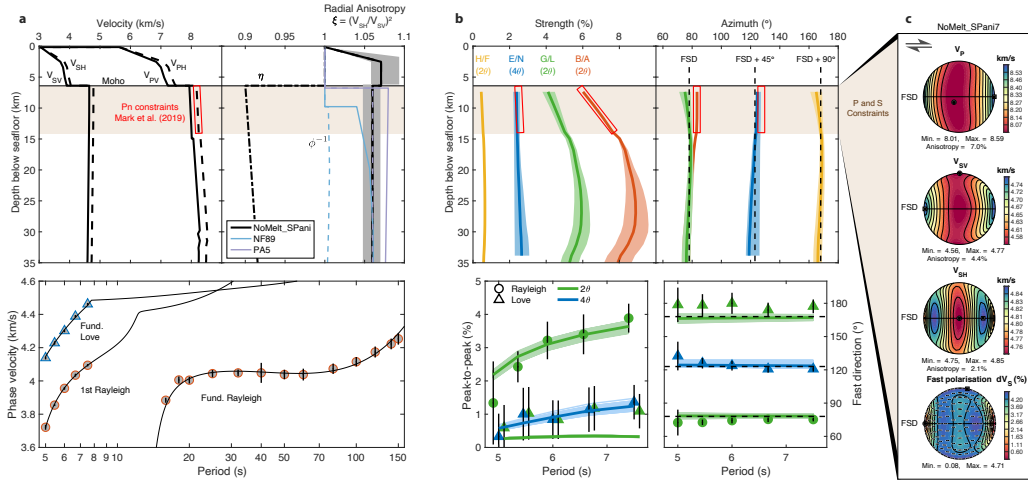
Figure 2. Comprehensive elastic model and data fit for the NoMelt region. Summary of the NoMelt_SPani model. (**a**), V_P, V_S, and Radial anisotropy ξ (solid) model and data fit after Russell et al. (2019). Grey shading for NoMelt radial anisotropy captures the range of models that fit the data, with the best fit model shown in black. Brown shading indicates where both V_P (Mark et al., 2019) and V_S constraints exist in the upper ~7 km of the mantle. NF89, (Nishimura & Forsyth, 1989) 52–110 Ma region; PA5, (Gaherty et al., 1996). (**b**), Azimuthal anisotropy strength and azimuth. Model uncertainties of two standard deviations from bootstrapping are shaded. Data fit and range of bootstrap model fits are shown in the lower panels. (**c**), Velocity calculations for the average elastic tensor for the upper ~7 km of the lithospheric mantle (NoMelt_SPani7), plotted using the MATLAB Seismic Anisotropy Toolkit (Walker & Wookey, 2012). The horizontal black line denotes the horizontal plane with the fossil-spreading direction (FSD) to the east and west. Maxima and minima are denoted by a square and circle, respectively. $dV_S = 200(V_{SH} - V_{SV})/(V_{SH} + V_{SV})$
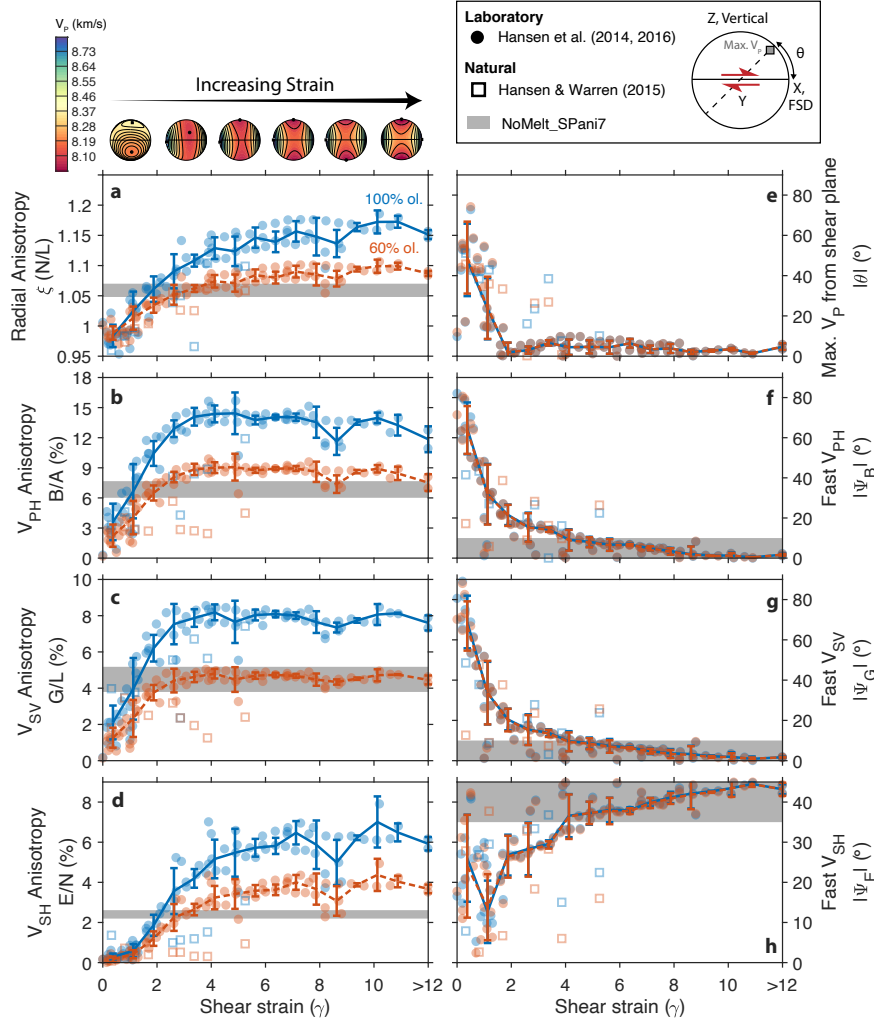
Figure 3. **NoMelt anisotropy compared with olivine petrofabric data as a function of shear strain and pyroxene content.** (**a–d**) Anisotropy strength and (**f–h**) fast azimuth with respect to the shear direction or FSD for laboratory (solid circles) (Hansen et al., 2014, 2016) and natural samples (open squares) (Hansen & Warren, 2015). The NoMelt seismic model for the upper ∼7 km of the lithospheric mantle, NoMelt_SPani7, is shown in grey with a width that represents the full range of values in that depth range. NoMelt FSD uncertainty is ∼10°. **e** Magnitude of the angle between maximum V_P and the shear plane; seismic model does not constrain this parameter. Calculations for (blue) pure olivine and (red) 60% olivine, 40% orthopyroxene are shown (see Methods for details on the inclusion of orthopyroxene). Error bars show median and standard deviation for laboratory data binned by strain with bin width $\gamma = 0.75$. V_P surfaces are shown above **a** for laboratory samples averaged by increments of $\gamma = 2$ (See also Figure S6). All samples oriented consistent with the seismic reference frame: shear plane parallel to Earth's surface and shear direction parallel to the FSD.
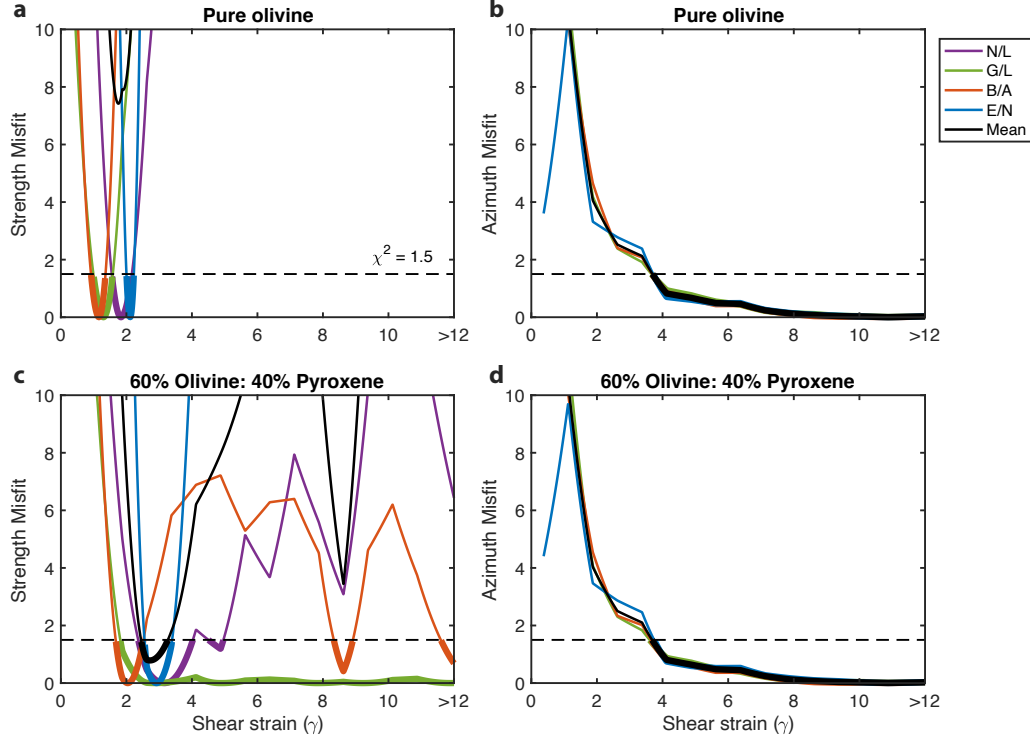
Figure 4. Misfit of anisotropy strength and fast azimuth with shear strain. (**a**) Misfit between the strength of anisotropy of NoMelt_SPani7 observations and experimental data from Figure 3, assuming 100% olivine. Line color indicates anisotropy type, where black is the average misfit value. Thick lines indicate values of misfit that are below the misfit threshold of $\chi^2 = 1.5$ (dashed line), meaning that the seismic observation and laboratory data agree. (**b**) same as (a) but for anisotropy fast azimuth. (**c,d**) same as (a,b) but for 60% olivine and 40% pyroxene. Misfit is calculated as $\chi^2 = (\bar{d}_{\mathrm{obs}} - \bar{d}_{\mathrm{exp}})^2/\sigma_{\mathrm{obs}}^2$, where $\bar{d}_{\mathrm{obs}}$ is the median observed value at Nomelt, $\bar{d}_{\mathrm{exp}}$ is the median experimental value, and σ_{obs} is the uncertainty on the observed value.
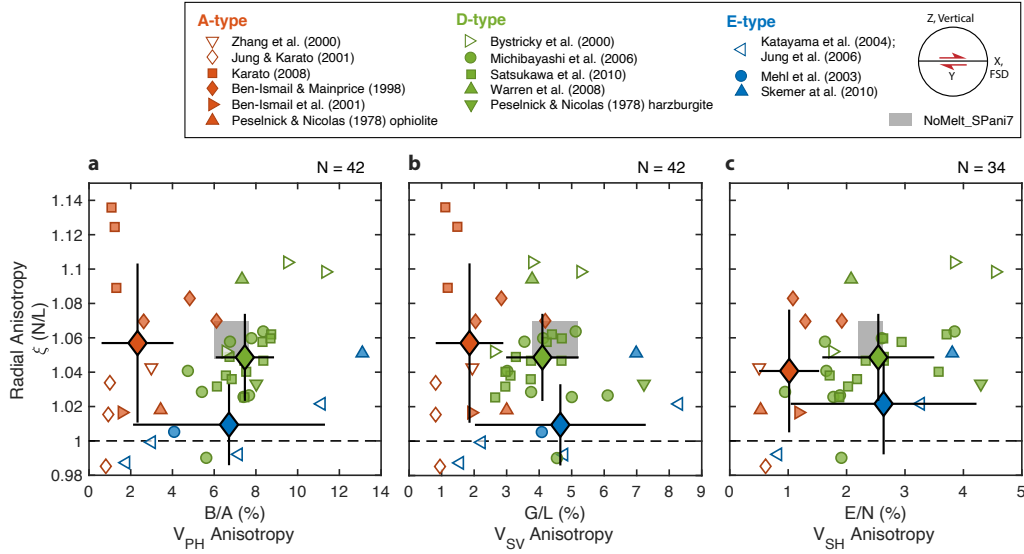
Figure 5. **Anisotropy of A-, D-, and E-type olivine LPO.** Radial anisotropy compared to (**a**) V_{PH}, (**b**) V_{SV}, and (**c**) V_{SH} azimuthal anisotropy for three fabric types compared to the NoMelt model, shown in grey. Open and closed symbols denote laboratory and natural samples, respectively. The large filled diamonds show the mean and one standard deviation for each fabric type. Effects of orthopyroxene are included assuming a composition of 75% olivine and 25% orthopyroxene by volume. No correction is applied to the samples from Peselnick & Nicolas (1978), which were derived ultrasonically and therefore already include the bulk chemistry. Note that (c) contains fewer data points than (a) and (b) due unreported V_{SH} anisotropy values for some studies.
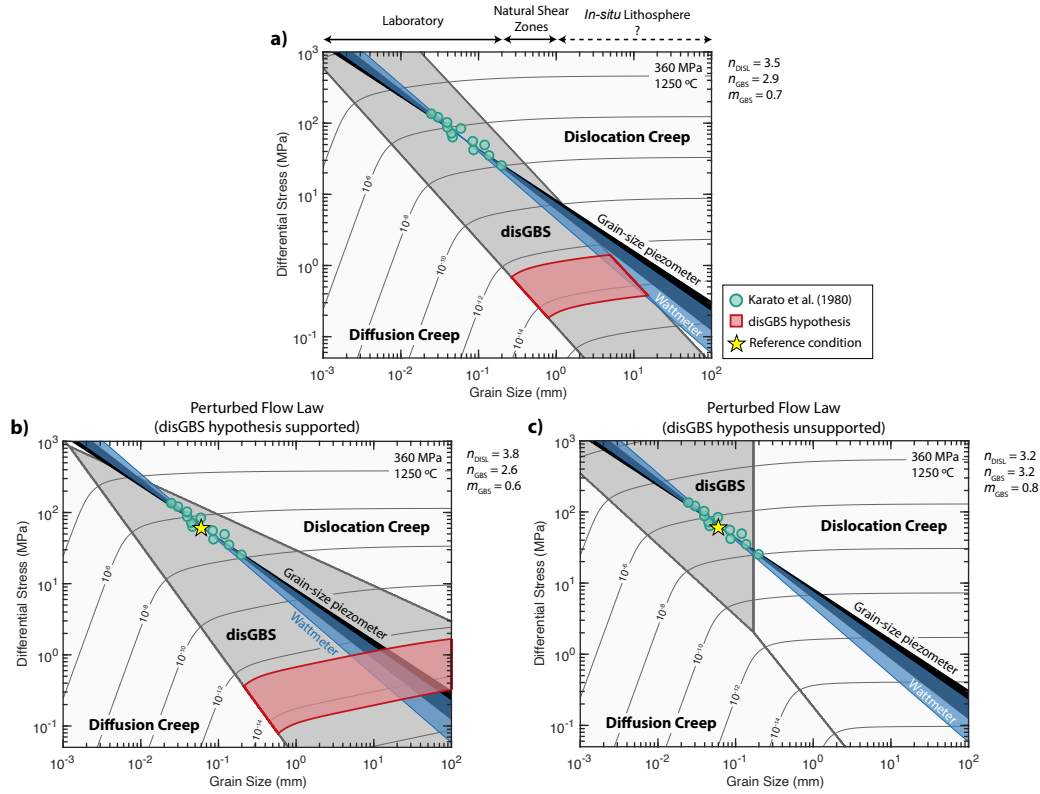
Figure 6. **Evaluation of the disGBS hypothesis for producing D-type LPO at mid-ocean ridge conditions.** (a) Strain rate contours are calculated using the nominal olivine flow laws of Hansen et al. (2011) at a temperature of $1250°C$ and pressure of 360 MPa (see Table S3), approximating shallow mantle conditions at the MOR. The red region bounded by strain rates of $10^{-14.5}$–$10^{-12.5}$ s^{-1} and within the grey dislocation-accomodated grain-boundary sliding (disGBS) regime represents the range of stress and grain sizes predicted by the disGBS hypothesis to produce D-type fabric (e.g. Braun, 2004; Warren et al., 2008). The grain-size wattmeter of Austin & Evans (2007) is shown in blue and includes uncertainties in laboratory derived stress and grain-size exponents (see Methods for details). A commonly used grain-size piezometer (Karato et al., 1980; Hirth & Kohlstedt, 2015) is shown in black. Laboratory data of Karato et al. (1980) are shown in teal. (**b**–**c**) same as a) but for perturbed flow-law parameters n_{DISL}, n_{GBS}, and m_{GBS} within their uncertainty bounds, representing endmember cases. The star marks the reference state ($d = 60$ μm, $\sigma = 60$ MPa) used to ensure agreement with laboratory data (See methods for details). Conditions in (b) support the disGBS hypothesis, while (c) does not.

Table 1. NoMelt_SPani7 elastic tensor, C_{ij}, averaged over the upper $\sim$7 km of the mantle. The tensor is oriented in the seismological reference frame with X parallel to the fossil-spreading direction, Y parallel to Earth's surface and perpendicular to fossil spreading, and Z perpendicular to Earth's surface.

i \ j	1	2	3	4	5	6
1	243.5427	71.5726	73.6646	0	0	1.5311
2	–	212.0492	74.4322	0	0	1.2569
3	–	–	213.2303	0	0	0.0068
4	–	–	–	68.5948	-0.0441	0
5	–	–	–	–	75.3675	0
6	–	–	–	–	–	74.4751

660 ## Appendix A Elastic parameter definitions

661   The five Love parameters A, C, L, N, and F (Dziewonski & Anderson, 1981; An-

662   derson & Dziewonski, 1982) that describe a transversely isotropic medium can be writ-

663   ten in terms of the elastic tensor C_{ij} as follows (Montagner & Nataf, 1986):

$$A = \rho V_{\mathrm{PH}}^2 = \frac{3}{8}(C_{11} + C_{22}) + \frac{1}{4}C_{12} + \frac{1}{2}C_{66}, \tag{A1}$$

$$C = \rho V_{\mathrm{PV}}^2 = C_{33}, \tag{A2}$$

$$L = \rho V_{\mathrm{SV}}^2 = \frac{1}{2}(C_{55} + C_{44}), \tag{A3}$$

$$N = \rho V_{\mathrm{SH}}^2 = \frac{1}{8}(C_{11} + C_{22}) - \frac{1}{4}C_{12} + \frac{1}{2}C_{66}, \tag{A4}$$

$$F = \rho\eta\,(V_{\mathrm{PH}}^2 - 2V_{\mathrm{SV}}^2) = \frac{1}{2}(C_{13} + C_{23}), \tag{A5}$$

$$\xi = \left(\frac{V_{\mathrm{SH}}}{V_{\mathrm{SV}}}\right)^2 = \frac{N}{L}, \tag{A6}$$

664   where radial anisotropy, ξ, is a proxy for vertical ($\xi < 1$) or horizontal ($\xi > 1$) flow in

665   the mantle.

666   In the case of a medium with orthorhombic symmetry, each elastic moduli varies

667   about its average value according to a sinusoid with magnitude (G, B, H, and E) and

668   corresponding azimuth (Ψ_G, Ψ_B, Ψ_H, and Ψ_E) of anisotropy:

2θ :

$$G = \delta L = \sqrt{G_{\mathrm{c}}^2 + G_{\mathrm{s}}^2}, \qquad \Psi_G = \frac{1}{2}\arctan\left(\frac{G_{\mathrm{s}}}{G_{\mathrm{c}}}\right); \tag{A7}$$

$$B = \delta A = \sqrt{B_{\mathrm{c}}^2 + B_{\mathrm{s}}^2}, \qquad \Psi_B = \frac{1}{2}\arctan\left(\frac{B_{\mathrm{s}}}{B_{\mathrm{c}}}\right); \tag{A8}$$

$$H = \delta F = \sqrt{H_{\mathrm{c}}^2 + H_{\mathrm{s}}^2}, \qquad \Psi_H = \frac{1}{2}\arctan\left(\frac{H_{\mathrm{s}}}{H_{\mathrm{c}}}\right); \tag{A9}$$

4θ :

$$E = \delta N = \sqrt{E_{\mathrm{c}}^2 + E_{\mathrm{s}}^2}, \qquad \Psi_E = \frac{1}{4}\arctan\left(\frac{-E_{\mathrm{s}}}{-E_{\mathrm{c}}}\right); \tag{A10}$$

$$G_{\mathrm{c}} = \frac{1}{2}(C_{55} - C_{44}), \tag{A11}$$

$$G_{\mathrm{s}} = C_{54}, \tag{A12}$$

$$B_{\mathrm{c}} = \frac{1}{2}(C_{11} - C_{22}), \tag{A13}$$

$$B_{\mathrm{s}} = C_{16} + C_{26}, \tag{A14}$$

$$H_{\mathrm{c}} = \frac{1}{2}(C_{13} - C_{23}), \tag{A15}$$

$$H_{\mathrm{s}} = C_{36}, \tag{A16}$$

$$E_{\mathrm{c}} = \frac{1}{8}(C_{11} + C_{22}) - \frac{1}{4}C_{12} - \frac{1}{2}C_{66}, \tag{A17}$$

$$E_{\mathrm{s}} = \frac{1}{2}(C_{16} - C_{26}), \tag{A18}$$

The magnitude and direction of azimuthal anisotropy depend on the bulk orientation and degree of organization of olivine [100] within the horizontal plane.

Appendix B Wattmeter steady-state grain size calculation

Grain-size evolution as a function of stress (σ) is estimated following the wattmeter approach of Austin & Evans (2007):

$$\dot{d} = \frac{K_{\mathrm{g}}}{p}d^{1-p}\exp\left(-\frac{E_{\mathrm{g}} + \bar{P}V_{\mathrm{g}}}{RT}\right) - \frac{2\chi}{c\gamma}d^2\boldsymbol{\sigma} : \dot{\boldsymbol{\varepsilon}}, \tag{B1}$$

where K_{g} and E_{g} are the grain growth prefactor and activation energy, respectively. The first term on the right-hand side represents grain growth by material diffusion between grains, and the second term represents grain-size reduction through dynamic recrystallization, which depends on χ the fraction of work done by dislocation mechanisms in order to change grain-boundary area, average specific grain-boundary energy, γ, and a geometric constant, c. We follow (Behn et al., 2009) and assume a grain growth exponent of $p = 3$. Assuming deformation occurs via disGBS, $\dot{\varepsilon} = A_{\mathrm{GBS}}\sigma^n d^{-m}\exp\left(-(E_{\mathrm{GBS}} + PV_{\mathrm{GBS}})/RT\right)$ and setting eq (B1) equal to zero, the steady-state grain size is given by:

$$d_{\mathrm{ss}} = \left[\frac{K_{\mathrm{g}}c\gamma}{2\chi p A_{\mathrm{GBS}}\sigma^{n+1}}\exp\left(\frac{(E_{\mathrm{GBS}} - E_{\mathrm{g}}) + (PV_{\mathrm{GBS}} - PV_{\mathrm{g}})}{RT}\right)\right]^{\frac{1}{1+p-m}} \tag{B2}$$

All parameter values can be found in Table S3. The resulting steady-state grain-size variation with stress, or wattmeter, at $T = 1250°C$ is shown in Figure 6.

–32–

Appendix C Flow-law uncertainties

Uncertainty in grain-size and stress exponents in olivine flow laws affect both the wattmeter calculation as well as deformation mechanism maps when extrapolated from laboratory to mantle conditions. We evaluate the effect of experimentally determined uncertainties in m_{GBS}, n_{GBS}, and n_{DISL} on the wattmeter and deformation mechanism maps by perturbing them within their uncertainty bounds ($n \pm 0.3$ and $m \pm 0.1$ relative to the reference values listed in Table S3). In order to remain consistent with the laboratory data, we correspondingly solve for prefactors A_{GBS} and A_{DISL} using the strain rate evaluated at a reference state of $d = 60$ μm and $\sigma = 60$ MPa, representative of average laboratory conditions. The deformation mechanism map and wattmeter are then calculated using the new value of A and perturbed values of n and m. The resulting effects on the deformation mechanism map, and the disGBS region in particular, are shown for two endmember cases in Figure 6b–c. Because we calculate the deformation mechanism maps and the grain size versus stress relationships at a temperature of 1250°C (which is within the temperature range that the grain-growth and deformation experiments were conducted), uncertainties in the activation energies for the flow laws and grain-growth law (Speciale et al., 2020) do not significantly impact our analysis. This flow-law exploration was implemented using the Very Broadband Rheology calculator (Havlin et al., 2021).

We perform a grid search over values of m_{GBS}, n_{GBS}, and n_{DISL} within their uncertainty bounds to determine the range of parameters that satisfy our *in situ* inference of disGBS as well as the laboratory derived grain-size piezometer and wattmeter (Figure C1). A set of parameters is considered acceptable if disGBS is predicted to occur at grain sizes at least as large as those predicted from the piezometer and wattmeter in Figure 6 (i.e., when the piezometer and wattmeter fall completely within the disGBS regime) at mantle strain rates of $10^{-14.5}$–$10^{-12.5}$ s^{-1}. Figure C1 shows that this criterion is met when m_{GBS} and n_{GBS} are smaller than their reference values and/or n_{DISL} is larger than its reference value. Furthermore, there is a clear tradeoff between the disGBS parameters (m_{GBS}, n_{GBS}) and the dislocation creep parameter n_{DISL}.
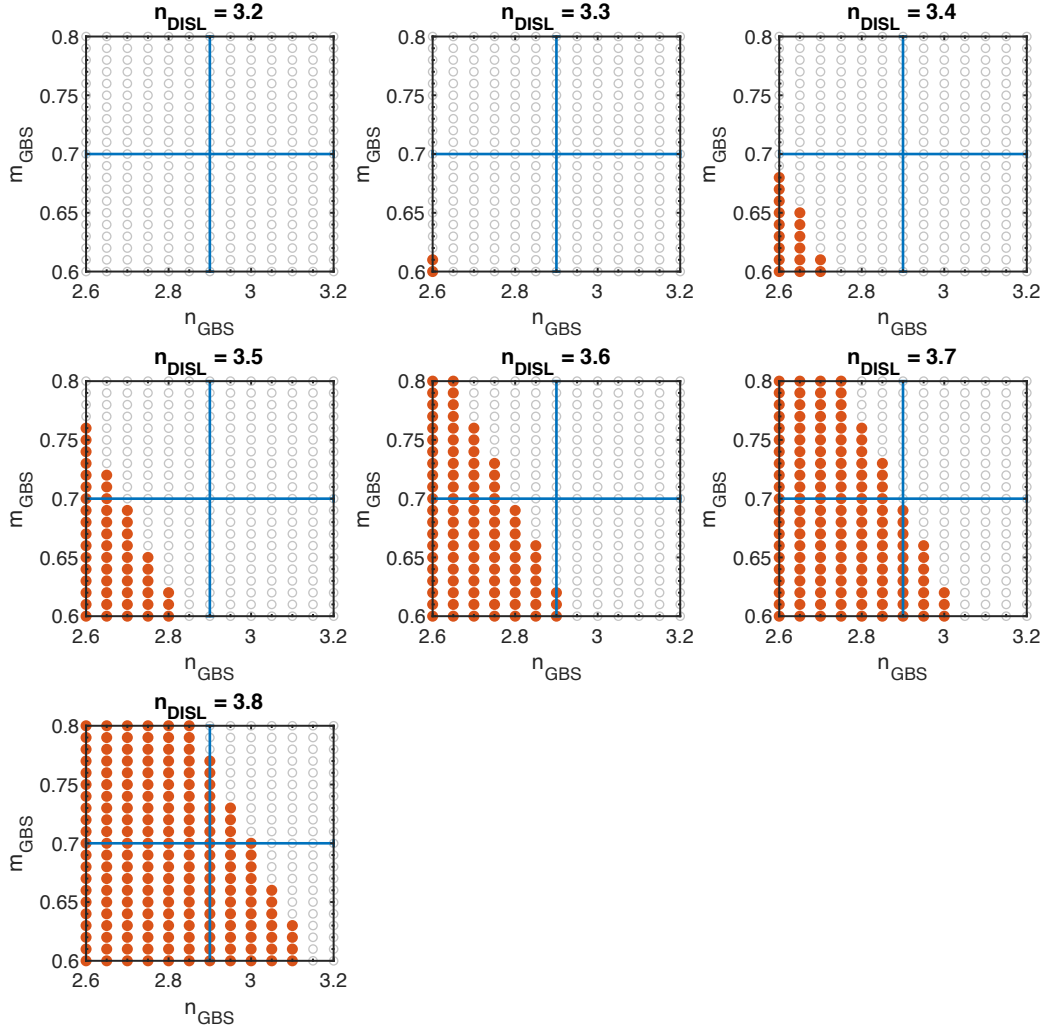
Figure C1. **Flow-law parameter combinations which predict disGBS at mantle strain rates.** A grid search is performed over values of n_{DISL}, n_{GBS}, and m_{GBS} within their uncertainty bounds in order to determine the combinations for which disGBS is predicted to occur at grain sizes corresponding to the piezometer and wattmeter shown in Figure 6 at mantle strain rates. A combination of parameters is considered acceptable when the grain-size piezometer and wattmeter are completely within the disGBS region of the deformation mechanism map for strain rates of $10^{-14.5}$–$10^{-12.5}$ s^{-1}. Filled red circles indicate parameter combinations for which this criterion is met, while open circles failed to meet this criterion. The vertical and horizontal blue lines indicate the reference values of n_{GBS} and m_{GBS}, respectively from Table S3. The reference value of n_{DISL} is 3.5. We find that smaller values of n_{GBS} and m_{GBS} and/or larger values of n_{DISL} relative to their reference values are compatible with the disGBS hypothesis.

Open Research

Seismic data was accessed through the IRIS Data Management Center under network code ZA using the open-source Python package ObsPy (`https://docs.obspy.org/`). Elastic tensors were manipulated and visualized using the MATLAB Seismic Anisotropy Toolkit (`https://geophysics.gly.bris.ac.uk/MSAT/`). Olivine flow laws were calculated using the Very Broadband Rheology calculator (`https://vbr-calc.github.io/vbr/`). The complete elastic models are included as Supplementary Tables S1 and S2 and all compiled sample data are included as Dataset files S1–S4. These files are also hosted at the following external repository: `https://doi.org/10.5281/zenodo.7079909`.

Acknowledgments

References

Abramson, E. H., Brown, J. M., Slutsky, L. J., & Zaug, J. (1997). The elastic constants of San Carlos olivine to 17 GPa. *Journal of Geophysical Research*, *102*(B6), 12253–12263. doi: 10.1029/97jb00682

Anderson, D. L., & Dziewonski, A. M. (1982). Upper mantle anisotropy: evidence from free oscillations. *Geophysical Journal of the Royal Astronomical Society*, *69*, 383–404.

Austin, N. J., & Evans, B. (2007). Paleowattmeters: A scaling relation for dynamically recrystallized grain size. *Geology*, *35*(4), 343–346. doi: 10.1130/G23244A.1

Bai, Q., Mackwell, S. J., & Kohlstedt, D. L. (1991). High-Temperature Creep of Olivine Single Crystals 1. Mechanical Results for Buffered Samples. *Journal of Geophysical Research*, *96*(B2), 2441–2463.

Bécel, A., Shillington, D. J., Nedimovi, M. R., Webb, S. C., & Kuehn, H. (2015). Origin of dipping structures in fast-spreading oceanic lower crust offshore Alaska imaged by multichannel seismic data. *Earth and Planetary Science Letters*, *424*,

745   26–37. doi: 10.1016/j.epsl.2015.05.016

746   Behn, M. D., Hirth, G., & Elsenbeck, J. R. (2009). Implications of grain size evo-

747   lution on the seismic structure of the oceanic upper mantle. *Earth and Planetary*

748   *Science Letters*, *282*(1-4), 178–189. Retrieved from `http://dx.doi.org/10.1016/`

749   `j.epsl.2009.03.014`   doi: 10.1016/j.epsl.2009.03.014

750   Ben-Ismail, W., Barruol, G., & Mainprice, D. (2001). The Kaapvaal craton seismic

751   anisotropy: Petrophysical analyses of upper mantle kimberlite nodules. *Geophysi-*

752   *cal Research Letters*, *28*(13), 2497–2500.

753   Ben-Ismail, W., & Mainprice, D. (1998). An olivine fabric database: An overview of

754   upper mantle fabrics and seismic anisotropy. *Tectonophysics*, *296*(1-2), 145–157.

755   doi: 10.1016/S0040-1951(98)00141-3

756   Bernard, R. E., Schulte-Pelkum, V., & Behr, W. M. (2021). The competing effects

757   of olivine and orthopyroxene CPO on seismic anisotropy. *Tectonophysics*, *814*,

758   228954. Retrieved from `https://doi.org/10.1016/j.tecto.2021.228954`   doi:

759   10.1016/j.tecto.2021.228954

760   Blackman, D. K., Boyce, D. E., Castelnau, O., Dawson, P. R., & Laske, G. (2017).

761   Effects of crystal preferred orientation on upper-mantle flow near plate bound-

762   aries: Rheologic feedbacks and seismic anisotropy. *Geophysical Journal Interna-*

763   *tional*, *210*, 1481–1493. doi: 10.1093/gji/ggx251

764   Blackman, D. K., Kendall, J., Paul, R. D., Wenk, H., Boyce, D., & Morgan, J. P.

765   (1996). Teleseismic imaging of subaxial flow at mid-ocean ridges : traveltime

766   effects of anisotropic mineral texture in the mantle. *Geophysical Journal Interna-*

767   *tional*, *127*, 415–426.

768   Bollinger, C., Marquardt, K., & Ferreira, F. (2019). Intragranular plasticity vs. grain

769   boundary sliding (GBS) in forsterite: Microstructural evidence at high pressures

770   (3.5-5.0 GPa). *American Mineralogist*, *104*, 220–231. doi: 10.2138/am-2019-6629

771   Braun, M. G. (2004). *Petrologic and microstructural constraints on focused melt*

772   *transport in dunites and the rheology of the shallow mantle* (Unpublished doctoral

773   dissertation). Massachesetts Institute of Technology.

774   Braun, M. G., Hirth, G., & Parmentier, E. M. (2000). The effects of deep damp

775   melting on mantle flow and melt generation beneath mid-ocean ridges. *Earth and*

776   *Planetary Science Letters*, *176*, 339–356. doi: 10.1016/S0012-821X(00)00015-7

777   Bystricky, M., Kunze, K., Burlini, L., & Burg, J. P. (2000). High shear strain of

778   olivine aggregates: Rheological and seismic consequences.   *Science*, *290*(5496),
779   1564–1567. doi: 10.1126/science.290.5496.1564

780 Castelnau, O., Blackman, D. K., Lebensohn, R. A., & Castañeda, P. P.   (2008).
781   Micromechanical modeling of the viscoplastic behavior of olivine.   *Journal of*
782   *Geophysical Research: Solid Earth*, *113*, 1–18. doi: 10.1029/2007JB005444

783 Connolly, J. A.   (2009).   The geodynamic equation of state: What and how.   *Geo-*
784   *chemistry, Geophysics, Geosystems*, *10*(10). doi: 10.1029/2009GC002540

785 Dick, H., & Natland, J.   (1996).   Late-Stage Melt Evolution and Transport in the
786   Shallow Mantle beneath the East Pacific Rise.   *Proceedings of the Ocean Drilling*
787   *Program, Scientific Results*, *147*, 103–134. doi: 10.2973/odp.proc.sr.147.007.1996

788 Dziewonski, A. M., & Anderson, D. L.   (1981).   Preliminary reference Earth model.
789   *Physics of the Earth and Planetary Interiors*, *25*, 297–356.

790 Faul, U. H.   (1997).   Permeability of partially molten upper mantle rocks from ex-
791   periments and percolation theory.   *Journal of Geophysical Research: Solid Earth*,
792   *102*(B5), 10299–10311. doi: 10.1029/96jb03460

793 Ferreira, F., Hansen, L. N., & Marquardt, K. (2021). The Effect of Grain Boundaries
794   on Plastic Deformation of Olivine.   *Journal of Geophysical Research: Solid Earth*,
795   *126*, 1–20. doi: 10.1029/2020JB020273

796 Forsyth, D. W.   (1975).   The Early Structural Evolution and Anisotropy of the
797   Oceanic Upper Mantle.   *Geophysical Journal of the Royal Astronomical Society*,
798   *43*(1), 103–162.

799 Gaherty, J. B., Jordan, T. H., & Gee, L. S.   (1996).   Seismic structure of the upper
800   mantle in a central Pacific corridor. *Journal of Geophysical Research*, *101*, 22,291–
801   22,309.

802 Gaherty, J. B., Lizarralde, D., Collins, J. A., Hirth, G., & Kim, S.   (2004).   Mantle
803   deformation during slow seafloor spreading constrained by observations of seismic
804   anisotropy in the western Atlantic.   *Earth and Planetary Science Letters*, *228*,
805   255–265. doi: 10.1016/j.epsl.2004.10.026

806 Hacker, B. R.   (2008).   H2O subduction beyond arcs.   *Geochemistry, Geophysics,*
807   *Geosystems*, *9*(3). doi: 10.1029/2007GC001707

808 Hansen, L. N., Faccenda, M., & Warren, J. M.   (2021).   A review of mechanisms
809   generating seismic anisotropy in the upper mantle. *Physics of the Earth and Plan-*
810   *etary Interiors*, *313*, 106662.   Retrieved from https://doi.org/10.1016/j.pepi

811   .2021.106662 doi: 10.1016/j.pepi.2021.106662

812 Hansen, L. N., & Warren, J. M.   (2015).   Quantifying the effect of pyroxene on de-

813   formation of peridotite in a natural shear zone.   *Journal of Geophysical Research:*

814   *Solid Earth*, *120*, 2717–2738. doi: 10.1002/2014JB011584.Received

815 Hansen, L. N., Warren, J. M., Zimmerman, M. E., & Kohlstedt, D. L.   (2016).

816   Viscous anisotropy of textured olivine aggregates, Part 1: Measurement of the

817   magnitude and evolution of anisotropy. *Earth and Planetary Science Letters*, *445*,

818   92–103. Retrieved from `http://dx.doi.org/10.1016/j.epsl.2016.04.008` doi:

819   10.1016/j.epsl.2016.04.008

820 Hansen, L. N., Zhao, Y. H., Zimmerman, M. E., & Kohlstedt, D. L.   (2014).   Pro-

821   tracted fabric evolution in olivine: Implications for the relationship among

822   strain, crystallographic fabric, and seismic anisotropy.   *Earth and Planetary*

823   *Science Letters*, *387*, 157–168.   Retrieved from `http://dx.doi.org/10.1016/`

824   `j.epsl.2013.11.009` doi: 10.1016/j.epsl.2013.11.009

825 Hansen, L. N., Zimmerman, M. E., & Kohlstedt, D. L.   (2011).   Grain boundary

826   sliding in San Carlos olivine: Flow law parameters and crystallographic-preferred

827   orientation.   *Journal of Geophysical Research: Solid Earth*, *116*(8), 1–16.   doi:

828   10.1029/2011JB008220

829 Havlin, C., Holtzman, B. K., & Hopper, E.   (2021).   Inference of thermodynamic

830   state in the asthenosphere from anelastic properties, with applications to North

831   American upper mantle.   *Physics of the Earth and Planetary Interiors*, *314*,

832   106639.   Retrieved from `https://doi.org/10.1016/j.pepi.2020.106639`   doi:

833   10.1016/j.pepi.2020.106639

834 Hess, H.   (1964).   Seismic Anisotropy of the Uppermost Mantle under Oceans.   *Na-*

835   *ture*, *203*, 629–631.

836 Hirth, G., & Kohlstedt, D. L.   (1995).   Experimental constraints on the dynamics of

837   the partially molten upper mantle 2. Deformation in the dislocation creep regime.

838   *Journal of Geophysical Research*, *100*(B8). doi: 10.1029/95jb01292

839 Hirth, G., & Kohlstedt, D. L. (2003). Rheology of the Upper Mantle and the Mantle

840   Wedge: A View from the Experimentalists. In *Inside the subduction factory: Geo-*

841   *physical monograph 138* (pp. 83–105).

842 Hirth, G., & Kohlstedt, D. L.   (2015).   The stress dependence of olivine creep

843   rate: Implications for extrapolation of lab data and interpretation of recrys-

tallized grain size. *Earth and Planetary Science Letters*, *418*, 20–26. Retrieved from http://dx.doi.org/10.1016/j.epsl.2015.02.013 doi: 10.1016/j.epsl.2015.02.013

Jung, H., & Karato, S.-i. (2001). Water-Induced Fabric Transitions in Olivine. *Science*, *293*, 1460–1464.

Jung, H., Katayama, I., Jiang, Z., Hiraga, T., & Karato, S.-i. (2006). Effect of water and stress on the lattice-preferred orientation of olivine. *Tectonophysics*, *421*, 1–22. doi: 10.1016/j.tecto.2006.02.011

Karato, S.-i. (2008). Insights into the nature of plume-asthenosphere interaction from central Pacific geophysical anomalies. *Earth and Planetary Science Letters*, *274*, 234–240. doi: 10.1016/j.epsl.2008.07.033

Karato, S.-i., Jung, H., Katayama, I., & Skemer, P. (2008). Geodynamic Significance of Seismic Anisotropy of the Upper Mantle : New Insights from Laboratory Studies. *Annual Review Earth and Planetary Sciences*, *36*, 59–95. doi: 10.1146/annurev.earth.36.031207.124120

Karato, S.-i., Toriumi, M., & Fujii, T. (1980). Dynamic recrystallization of olivine single crystals during high-temperature creep. *Geophysical Research Letters*, *7*(9), 649–652.

Karato, S.-i., & Wu, P. (1993). *Rheology of the upper mantle: a synthesis.* (Vol. 260) (No. 5109). doi: 10.1126/science.260.5109.771

Karson, J. A., Collins, J. A., & Casey, J. F. (1984). Geologic and seismic velocity structure of the crust/mantle transition in the Bay of Islands ophiolite complex. *Journal of Geophysical Research*, *89*, 6126–6138.

Katayama, I., Jung, H., & Karato, S.-i. (2004). New type of olivine fabric from deformation experiments at modest water content and low stress. *Geology*, *32*(12), 1045–1048. doi: 10.1130/G20805.1

Kim, N., Ando, A., Yabe, K., & Hiraga, T. (2022). Olivine Morphology and Fabric During Diffusion Creep: Pure Shear Experiments. *Journal of Geophysical Research: Solid Earth*, *127*(5). doi: 10.1029/2021JB023613

Kodaira, S., Fujie, G., Yamashita, M., Sato, T., Takahashi, T., & Takahashi, N. (2014). Seismological evidence of mantle flow driving plate motions at a palaeo-spreading centre. *Nature Geoscience*, *7*(5), 371–375. doi: 10.1038/ngeo2121

Kumamoto, K. M., Warren, J. M., & Hansen, L. N. (2019). Evolution of the

Josephine Peridotite Shear Zones: 2. Influences on Olivine CPO Evolution. *Journal of Geophysical Research: Solid Earth*, *124*(12), 12763–12781. doi: 10.1029/2019JB017968

Lin, P.-Y. P., Gaherty, J. B., Jin, G., Collins, J. A., Lizarralde, D., Evans, R. L., & Hirth, G. (2016). High-resolution seismic constraints on flow dynamics in the oceanic asthenosphere. *Nature*, *535*(7613), 1–9. Retrieved from `http://www.nature.com/doifinder/10.1038/nature18012` doi: 10.1038/nature18012

Linckens, J., Herwegh, M., Mntener, O., & Mercolli, I. (2011). Evolution of a polymineralic mantle shear zone and the role of second phases in the localization of deformation. *Journal of Geophysical Research: Solid Earth*, *116*(6), 1–21. doi: 10.1029/2010JB008119

Liu, S., Tommasi, A., Vauchez, A., & Mazzucchelli, M. (2019). Crust-mantle coupling during continental convergence and break-up: Constraints from peridotite xenoliths from the Borborema Province, northeast Brazil. *Tectonophysics*, *766*, 249–269. Retrieved from `https://doi.org/10.1016/j.tecto.2019.05.017` doi: 10.1016/j.tecto.2019.05.017

Mainprice, D., & Silver, P. G. (1993). Interpretation of SKS-waves using samples from the subcontinental lithosphere. *Physics of the Earth and Planetary Interiors*, *78*, 257–280. doi: 10.1016/0031-9201(93)90160-B

Mark, H. F., Lizarralde, D., Collins, J. A., Miller, N. C., Hirth, G., Gaherty, J. B., & Evans, R. L. (2019). Azimuthal Seismic Anisotropy of 70-Ma Pacific-Plate Upper Mantle. *Journal of Geophysical Research: Solid Earth*, *124*, 1889–1909. doi: 10.1029/2018JB016451

Mehl, L., Hacker, B., Hirth, G., & Kelemen, P. B. (2003). Arc-parallel flow within the mantle wedge: Evidence from the accreted Talkeetna arc, south central Alaska. *Journal of Geophysical Research*, *108*(B8). doi: 10.1029/2002jb002233

Michibayashi, K., Ina, T., & Kanagawa, K. (2006). The effect of dynamic recrystallization on olivine fabric and seismic anisotropy: Insight from a ductile shear zone, Oman ophiolite. *Earth and Planetary Science Letters*, *244*, 695–708. doi: 10.1016/j.epsl.2006.02.019

Michibayashi, K., Mainprice, D., Fujii, A., Uehara, S., Shinkai, Y., Kondo, Y., ... Ji, S. (2016). Natural olivine crystal-fabrics in the western Pacific convergence region : A new method to identify fabric type. *Earth and Planetary Science Letters*, *443*,

70–80. Retrieved from `http://dx.doi.org/10.1016/j.epsl.2016.03.019` doi: 10.1016/j.epsl.2016.03.019

Miyazaki, T., Sueyoshi, K., & Hiraga, T. (2013). Olivine crystals align during diffusion creep of Earth's upper mantle. *Nature*, *502*(7471), 321–326. doi: 10.1038/nature12570

Montagner, J. P., & Anderson, D. L. (1989). Petrological constraints on seismic anisotropy. *Physics of the Earth and Planetary Interiors*, *54*, 82–105.

Montagner, J. P., & Nataf, H. C. (1986). A simple method for inverting the azimuthal anisotropy of surface waves. *Journal of Geophysical Research*, *91*, 511–520.

Montagner, J. P., & Tanimoto, T. (1991). Global Upper Mantle Tomography of Seismic Velocities and Anisotropies. *JGR*, *96*(9), 20,337–20,351.

Nishimura, C. E., & Forsyth, D. W. (1989). The Anisotropic Structure of the Upper Mantle in the Pacific Ocean. *Geophysical Journal of the Royal Astronomical Society*, *96*(2), 203–229.

Niu, Y., & Hékinian, R. (1997). Basaltic liquids and harzburgitic residues in the Garrett Transform: A case study at fast-spreading ridges. *Earth and Planetary Science Letters*, *146*, 243–258. doi: 10.1016/s0012-821x(96)00218-x

Pallister, J. S., & Hopson, C. A. (1981). Samail ophiolite plutonic suite: field relations, phase variation, cryptic variation and layering, and a model of a spreading ridge magma chamber. *Journal of Geophysical Research*, *86*(B4), 2593–2644. doi: 10.1029/JB086iB04p02593

Peselnick, L., & Nicolas, A. (1978). Seismic Anisotropy in an Ophiolite Peridotite: Application to Oceanic Upper Mantle. *Journal of Geophysical Research*, *83*(B3), 1227–1235.

Qi, C., Hansen, L. N., Wallis, D., Holtzman, B. K., & Kohlstedt, D. L. (2018). Crystallographic Preferred Orientation of Olivine in Sheared Partially Molten Rocks: The Source of the "a-c Switch". *Geochemistry, Geophysics, Geosystems*, *19*, 316–336. doi: 10.1002/2017GC007309

Russell, J. B., Gaherty, J. B., Lin, P. Y. P., Lizarralde, D., Collins, J. A., Hirth, G., & Evans, R. L. (2019). High-Resolution Constraints on Pacific Upper Mantle Petrofabric Inferred From Surface-Wave Anisotropy. *Journal of Geophysical Research: Solid Earth*, *124*, 631–657. doi: 10.1029/2018JB016598

Satsukawa, T., Michibayashi, K., Raye, U., Anthony, E. Y., Pulliam, J., & Stern, R. (2010). Uppermost mantle anisotropy beneath the southern Laurentian margin: Evidence from Knippa peridotite xenoliths, Texas. *Geophysical Research Letters*, *37*, L20312. doi: 10.1029/2010GL044538

Signorelli, J., & Tommasi, A. (2015). Modeling the effect of subgrain rotation recrystallization on the evolution of olivine crystal preferred orientations in simple shear. *Earth and Planetary Science Letters*, *430*, 356–366. Retrieved from `http://dx.doi.org/10.1016/j.epsl.2015.08.018` doi: 10.1016/j.epsl.2015.08.018

Skemer, P., Warren, J. M., & Hirth, G. (2012). The influence of deformation history on the interpretation of seismic anisotropy. *Geochemistry, Geophysics, Geosystems*, *13*(3), 1–10. doi: 10.1029/2011GC003988

Skemer, P., Warren, J. M., Kelemen, P. B., & Hirth, G. (2010). Microstructural and rheological evolution of a mantle shear zone. *Journal of Petrology*, *51*(1-2), 43–53. doi: 10.1093/petrology/egp057

Smewing, J. D. (1981). Mixing characteristics and compositional differences in mantle-derived melts beneath spreading axes: Evidence from cyclically layered rocks in the ophiolite of North Oman. *Journal of Geophysical Research: Solid Earth*, *86*(B4), 2645–2659. doi: 10.1029/jb086ib04p02645

Speciale, P. A., Behr, W. M., Hirth, G., & Tokle, L. (2020). Rates of Olivine Grain Growth During Dynamic Recrystallization and Postdeformation Annealing. *Journal of Geophysical Research: Solid Earth*, *125*(11). doi: 10.1029/2020JB020415

Stixrude, L., & Lithgow-Bertelloni, C. (2011). Thermodynamics of mantle minerals - II. Phase equilibria. *Geophysical Journal International*, *184*(3), 1180–1213. doi: 10.1111/j.1365-246X.2010.04890.x

Takeo, A., Kawakatsu, H., Isse, T., Nishida, K., Shiobara, H., Sugioka, H., . . . Utada, H. (2018). In Situ Characterization of the Lithosphere-Asthenosphere System beneath NW Pacific Ocean Via Broadband Dispersion Survey With Two OBS Arrays. *Geochemistry, Geophysics, Geosystems*, *19*. doi: 10.1029/2018GC007588

Tommasi, A. (1998). Forward modeling of the development of seismic anisotropy in the upper mantle. *Earth and Planetary Science Letters*, *160*, 1–13.

Tommasi, A., Godard, M., Coromina, G., Dautria, J. M., & Barsczus, H. (2004). Seismic anisotropy and compositionally induced velocity anomalies in the litho-

sphere above mantle plumes: A petrological and microstructural study of mantle xenoliths from French Polynesia. *Earth and Planetary Science Letters*, *227*, 539–556. doi: 10.1016/j.epsl.2004.09.019

Tommasi, A., Mainprice, D., Canova, G., & Chastel, Y. (2000). Viscoplastic self-consistent and equilibrium-based modeling of olivine lattice preferred orientations: Implications for the upper mantle seismic anisotropy. *Journal of Geophysical Research*, *105*, 7893–7908.

Tommasi, A., Mameri, L., & Godard, M. (2020). Textural and Compositional Changes in the Lithospheric Mantle Atop the Hawaiian Plume: Consequences for Seismic Properties. *Geochemistry, Geophysics, Geosystems*, *21*, 1–29. doi: 10.1029/2020GC009138

Tommasi, A., & Vauchez, A. (2015). Heterogeneity and anisotropy in the lithospheric mantle. *Tectonophysics*, *661*, 11–37. Retrieved from http://dx.doi.org/10.1016/j.tecto.2015.07.026 doi: 10.1016/j.tecto.2015.07.026

Toomey, D. R., Jousselin, D., Dunn, R. A., Wilcock, W. S. D., & Detrick, R. S. (2007). Skew of mantle upwelling beneath the East Pacific Rise governs segmentation. *Nature*, *446*, 409–414. doi: 10.1038/nature05679

Turner, A. J., Katz, R. F., & Behn, M. D. (2015). Grain-size dynamics beneath mid-ocean ridges: Implications for permeability and melt extraction. *Geochemistry, Geophysics, Geosystems*, *16*, 925–946. doi: 10.1002/2014GC005692.Received

Turner, A. J., Katz, R. F., Behn, M. D., & Keller, T. (2017). Magmatic Focusing to Mid-Ocean Ridges: The Role of Grain-Size Variability and Non-Newtonian Viscosity. *Geochemistry, Geophysics, Geosystems*, *18*(12), 4342–4355. doi: 10.1002/2017GC007048

Vonlanthen, P., Kunze, K., Burlini, L., & Grobety, B. (2006). Seismic properties of the upper mantle beneath Lanzarote (Canary Islands): Model predictions based on texture measurements by EBSD. *Tectonophysics*, *428*, 65–85. doi: 10.1016/j.tecto.2006.09.005

Walker, A. M., & Wookey, J. (2012). Computers & Geosciences MSAT – A new toolkit for the analysis of elastic and seismic anisotropy. *Computers and Geosciences*, *49*, 81–90. Retrieved from http://dx.doi.org/10.1016/j.cageo.2012.05.031 doi: 10.1016/j.cageo.2012.05.031

Warren, J. M. (2016). Global variations in abyssal peridotite compositions. *Lithos*,

¹⁰⁰⁹ *248-251*, 193–219. Retrieved from `http://dx.doi.org/10.1016/j.lithos.2015`

¹⁰¹⁰ `.12.023` doi: 10.1016/j.lithos.2015.12.023

¹⁰¹¹ Warren, J. M., Hirth, G., & Kelemen, P. B. (2008). Evolution of olivine lattice pre-

¹⁰¹² ferred orientation during simple shear in the mantle. *Earth and Planetary Science*

¹⁰¹³ *Letters*, *272*(3-4), 501–512. Retrieved from `http://dx.doi.org/10.1016/j.epsl`

¹⁰¹⁴ `.2008.03.063` doi: 10.1016/j.epsl.2008.03.063

¹⁰¹⁵ Yabe, K., & Hiraga, T. (2020). Grain-Boundary Diffusion Creep of Olivine:

¹⁰¹⁶ 2. Solidus Effects and Consequences for the Viscosity of the Oceanic Upper

¹⁰¹⁷ Mantle. *Journal of Geophysical Research: Solid Earth*, *125*(8), 1–22. doi:

¹⁰¹⁸ 10.1029/2020JB019416

¹⁰¹⁹ Zhang, S., ichiro Karato, S., Fitz Gerald, J., Faul, U. H., & Zhou, Y. (2000). Sim-

¹⁰²⁰ ple shear deformation of olivine aggregates. *Tectonophysics*, *316*, 133–152. doi: 10

¹⁰²¹ .1016/S0040-1951(99)00229-2

¹⁰²² Zhang, S., & Karato, S.-i. (1995). Lattice preferred orientation of olivine aggregates

¹⁰²³ deformed in simple shear. *Nature*, *375*, 774–777.